Astronomy & Astrophysics manuscript no. 29593JN
June 28, 2021

New outburst of the symbiotic nova AG Peg after 165 years

A. Skopal[1], S. Yu. Shugarov[1,2], M. Sekeráš[1], M. Wolf[3], T. N. Tarasova[4], F. Teyssier[5], M. Fujii[6], J. Guarro[7], O. Garde[8], K. Graham[9], T. Lester[10], V. Bouttard[11], T. Lemoult[12], U. Sollecchia[13], J. Montier[14], and D. Boyd[15]

[1] Astronomical Institute, Slovak Academy of Sciences, 059 60 Tatranská Lomnica, Slovakia
[2] Sternberg Astronomical Institute, Moscow State University, Universitetskij pr., 13, Moscow, 119991, Russia
[3] Astronomical Institute, Charles University Prague, CZ-180 00 Praha 8, V Holešovičkách 2, The Czech Republic
[4] Crimean Astrophysical Observatory, 298409 Nauchny, Crimea, Russia
[5] 67 Rue Jacques Daviel, Rouen 76100, France
[6] Fujii Kurosaki Observatory, 4500 Kurosaki, Tamashima, Kurashiki, Okayama 713-8126, Japan
[7] Balmes 2, 08784 PIERA, Barcelona, Spain
[8] Observatoire de la Tourbière, 38690 Chabons, France
[9] 23746 Schoolhouse Road, Manhattan, Illinois, USA 60442
[10] 1178 Mill Ridge Road, Arnprior, ON, K7S3G8, Canada
[11] 21 rue de Guémar, 68000 Colmar, France
[12] Chelles Observatory, 23 avenue hénin, 77500 Chelles, France
[13] Via dei Malatesta 10, 67100 LAquila, Italy
[14] 30 rue de la Boulais - 35000 Rennes, France
[15] West Challow Observatory, Oxfordshire OX12 9TX, UK

Received / Accepted

ABSTRACT

Context. AG Peg is known as the slowest symbiotic nova, which experienced its nova-like outburst around 1850. After 165 years, during June of 2015, it erupted again showing characteristics of the Z And-type outburst.
Aims. The primary objective is to determine basic characteristics, the nature and type of the 2015 outburst of AG Peg.
Methods. We achieved this aim by modelling the spectral energy distribution using low-resolution spectroscopy (330–750 nm; R = 500–1000), medium-resolution spectroscopy (420–720 nm; $R \sim 11000$), and $UBVR_{\rm C}I_{\rm C}$ photometry covering the 2015 outburst with a high cadence. Optical observations were complemented with the archival *HST* and *FUSE* spectra from the preceding quiescence.
Results. During the outburst, the luminosity of the hot component was in the range of $2–11\times10^{37}\,(d/0.8\,{\rm kpc})^2\,{\rm erg\,s^{-1}}$, being in correlation with the light curve (*LC*) profile. To generate the maximum luminosity by the hydrogen burning, the white dwarf (WD) had to accrete at $\sim 3\times10^{-7}\,M_\odot\,{\rm yr^{-1}}$, which exceeds the stable-burning limit and thus led to blowing optically thick wind from the WD. We determined its mass-loss rate to a few $\times10^{-6}\,M_\odot\,{\rm yr^{-1}}$. At the high temperature of the ionising source, $1.5 – 2.3\times10^5$ K, the wind converted a fraction of the WD's photospheric radiation into the nebular emission that dominated the optical. A one order of magnitude increase of the emission measure, from a few $\times10^{59}\,(d/0.8\,{\rm kpc})^2\,{\rm cm^{-3}}$ during quiescence, to a few $\times10^{60}\,(d/0.8\,{\rm kpc})^2\,{\rm cm^{-3}}$ during the outburst, caused a 2 mag brightening in the *LC*, which is classified as the Z And-type of the outburst.
Conclusions. The very high nebular emission and the presence of a disk-like H I region encompassing the WD, as indicated by a significant broadening and high flux of the Raman-scattered O VI 6825 Å line during the outburst, is consistent with the ionisation structure of hot components in symbiotic stars during active phases.

Key words. Stars: binaries: symbiotic – novae, cataclysmic variables – Stars: individual: AG Peg

1. Introduction

Symbiotic stars are the widest interacting binary systems comprising a cool giant as the donor star and a hot compact star, mostly a white dwarf (WD), accreting from the giant's wind (Mürset & Schmid 1999). Their orbital periods run from hundreds of days (S-type systems containing a normal giant) to a few times 10–100 years (D-type systems containing a Mira variable surrounded by a dust shell). The accreting WD represents a strong source of the extreme ultraviolet radiation ($T_{\rm h} \gtrsim 10^5$ K, $L_{\rm h} \sim 10^1 – 10^4\,L_\odot$) in the binary that ionises a fraction of the wind from the giant giving rise to the nebular emission (e.g. Seaquist et al. 1984, hereafter STB). This configuration represents the so-called *quiescent phase*, during which the symbiotic system releases its energy approximately at a constant rate and temperature. The observed luminosities of accreting WDs are powered by two main sources of the energy. In rare cases, low luminosities of $\sim 10^1 – 10^2\,L_\odot$ are generated solely by the accretion process onto the WD (e.g. EG And, 4 Dra, SU Lyn, see Skopal 2005a; Mukai et al. 2016), when its gravitational potential energy is converted into the radiation by the disk. In most cases, high luminosities of a few times $10^3\,L_\odot$ (e.g. Mürset et al. 1991; Skopal 2005b) are generated by stable nuclear hydrogen burning on the WD surface, which requires a certain range of accretion rates (Tutukov & Yungel'son 1976; Paczyński & Żytkow 1978).

Sometimes, the symbiotic system changes its radiation significantly, brightens up in the optical by a few magnitudes and shows signatures of a mass-outflow. We name this stage as the *active phase*. According to the brightness variation we distinguish two subclasses: (i) The 'Z And-type' outbursts with amplitudes of 1–3 mag in the optical, evolving on the timescale of weeks to years. This type of outburst can result from an increase

in the accretion rate above that sustaining the stable burning, which leads to expansion of the burning envelope simulating an A–F type pseudophotosphere (Tutukov & Yungel'son 1976; Paczyński & Rudak 1980). (ii) The nova-like outbursts with amplitudes > 3 mag that, after prolonged accretion by the WD from the giant's wind, undergo a thermonuclear outburst. Depending on the WD mass and the accretion rate we observe either very slow novae, whose outbursts last for dozens of years, or very fast novae lasting for several days to months and recurring during several years to decades (see modelling by Livio et al. 1989; Hachisu & Kato 2001; Yaron et al. 2005). The former are called 'symbiotic novae' whereas the latter are known as 'symbiotic recurrent novae'. Their properties have been discussed by many authors (e.g. Allen 1980; Mürset & Nussbaumer 1994; Munari 1997; Mikolajewska 2011).

AG Peg is a symbiotic binary comprising a M3 III giant (Kenyon & Fernández-Castro 1987) and a WD on an 818-d orbit (e.g. Fekel et al. 2000). This is a bright ($V \approx 8.5$), and thus a well studied object. Measuring its light variations from before 1850 (see Fig. 1 of Boyarchuk 1967) allowed for its classification as a symbiotic nova (Allen 1980). The outburst began in 1850 (Lundmark 1921) when it rose in brightness from $\sim$ 9 to reach a maximum of $\sim$ 6 mag around 1885. Afterwards, AG Peg followed a gradual decline to around 2000, and then, varying between 8.5 and 9.0 mag in V, kept its brightness until June 2015. Such an evolution of the *LC* together with other spectrophotometric parameters represents the slowest nova outburst ever recorded (Kenyon et al. 1993).

The evolution of luminosity and temperature of the burning WD during the whole outburst was described by Mürset & Nussbaumer (1994) and Altamore & Cassatella (1997). The peak luminosity, reached during 1940-50, was followed with a gradual decline to 1993 along a slowly increasing temperature. The following study by Kenyon et al. (2001) confirmed the continuing slow decline of the AG Peg luminosity by a factor of 2–3 from 1980–1985 to 1997.

Similar behaviour was indicated in the mass-loss rate from the hot component, $\dot{M}_{\rm h}$. Based on radio observations performed during 1973–75, Gregory & Kwok (1977) estimated $\dot{M}_{\rm h} = 10^{-6}\,M_\odot\,{\rm yr}^{-1}$. Using the radio flux at 5 GHz from 1984–87, Kenny et al. (1991) estimated an upper limit of $\dot{M}_{\rm h}$ to $1.1 \times 10^{-6}\,M_\odot\,{\rm yr}^{-1}$. During 1978–1993, a decline in $\dot{M}_{\rm h}$ from $\sim 10^{-6}$ to $(2-3)\times10^{-7}\,M_\odot\,{\rm yr}^{-1}$ was suggested by Kenyon et al. (1993).

The presence of strong winds from both the binary components was often used to identify main emission regions in AG Peg within the colliding winds model (e.g. Tomov 1993; Contini 1997, 2003; Tomov & Tomova 2001; Eriksson et al. 2004; Kenny & Taylor 2007). The most direct indication of colliding winds in AG Peg is the detection of X-ray emission from a very hot, optically thin plasma (Mürset et al. 1995). According to the gradual decrease of the hot component luminosity, Zamanov & Tomov (1995) predicted that the colliding-wind stage would end between 1999 and 2004, and accretion from the wind would recommence. From around 1997 to June 2015, AG Peg kept its brightness at a constant level, showing just pronounced wave-like orbitally-related variations (Skopal et al. 2007, 2012, this paper) – the main characteristic of the quiescent phase of a symbiotic star.

During June 2015, AG Peg experienced a new outburst (AAVSO Alert Notice 521 [1]). On July 1, 2015, Steele et al. (2015) indicated strong emission lines of, namely, H I, He II, and N III superposed on nebular continuum with a pronounced Balmer jump in emission on their low-resolution spectrum (320–620 nm). Around a maximum of the optical brightness, from June 28 to July 8, 2015, the Swift/XRT observation detected an increase in the count rate with a factor of ~3 with respect to the previous observation on August 16–19, 2013 (Nuñez & Luna 2013; Luna et al. 2015). Following Swift/XRT, monitoring of the 2015 outburst indicated a markedly variable X-ray flux on a time scale of days (Ramsay et al. 2015, 2016). The authors ascribed the origin of the strong and variable X-rays to shocks in the variable ejecta. Analysing the same Swift/XRT observations, Zhekov & Tomov (2016) came to the conclusion that the characteristics of the X-ray emission from the 2015 outburst could not result from colliding stellar winds in a binary system as was indicated by previous *ROSAT* observations from June of 1993. Using optical spectroscopy and *BV* photometry, Tomov et al. (2016) concluded that the 2015 outburst of AG Peg places it among the classical Z And-type symbiotic binary systems.

In this contribution we determine basic characteristics and the nature of the 2015 AG Peg outburst using a high cadence optical spectroscopy and multicolour $UBVR_{\rm C}I_{\rm C}$ photometry complemented with ultraviolet spectra from the preceding quiescence. In Sect. 2 we summarise and describe our observations and data reduction. Section 3 describes our analysis and presents the results. Their discussion and summary are found in Sects. 4 and 5, respectively.

2. Observations

2.1. Photometry

Multicolour photometric observations were carried out with two 60cm, f/12.5 Cassegrain telescopes at the Stará Lesná Observatory (G1 and G2 observing pavilions) operated by the Astronomical Institute of the Slovak Academy of Sciences.

1. CCD photometry (G1 pavilion) was obtained in the standard Johnson-Cousins $UBVR_{\rm C}I_{\rm C}$ system using the *FLI ML3041* CCD camera (2048×2048 px, pixel size: 15 μm ×15 μm, scale: 0.4 arcsec/px, FoV: $14' \times 14'$), mounted at the Cassegrain focus. The data were reduced using the *IRAF* software package[2] as described by Parimucha & Vaňko (2005). All frames were dark-subtracted, flat-fielded and corrected for cosmic rays. Corresponding magnitudes were obtained using the comparison stars "a", "b", and "c" of Henden & Munari (2006). To get a better coverage, we complemented our CCD measurements with those from the AAVSO database [3].

2. Photoelectric UBV photometry was carried out in the G2 pavilion by a single-channel photometer mounted in the Cassegrain focus (see Vaňko et al. 2015a,b, in detail). The star HD 207 933 ($V = 8.10$, $B - V = 1.05$, $U - B = 0.97$) was used as the comparison star. Internal uncertainties of these one-day-mean measurements are of a maximum of a few ×0.01 mag in U, but smaller in other filters. Our photometric measurements are summarised in Table 1.

Multicolour photometry was used mainly to convert the relative and/or arbitrary flux units of the low-resolution and/or the medium-resolution spectra to absolute fluxes. To obtain flux-points of the true continuum, we determined corrections for emission lines by using our low-resolution spectra (see Skopal 2007). Magnitudes were converted to fluxes according to the calibration of Henden & Kaitchuck (1982) and Bessel (1979).

[1] https://www.aavso.org/aavso-alert-notice-521

[2] http://iraf.noao.edu

[3] https://www.aavso.org/data-download

2.2. Spectroscopy

Spectroscopic observations were secured at different observatories and/or private stations:

(i) At the Stará Lesná Observatory in the G1 observing pavilion with a 0.6 m Cassegrain telescope equipped with an eShel fiber-fed spectrograph (Shelyak; optical fiber of 50 μm) mounted at the f/5 focus. The detector was an ATIK 460EX CCD camera using 2750×2200 chip with 4.54 μm square pixels and 2×2 binning. Reduction of the spectroscopy was performed using dedicated scripts written using the *IRAF* package tasks, Linux shell scripts, and *FORTRAN* programs (see Pribulla et al. 2015).

(ii) At the Ondřejov Observatory, medium-resolution spectroscopy was performed using the coude single dispersion slit spectrograph of 2 m reflector and the BROR CCD camera with the SITe-005 800×2030 pixels chip. The resolution power at the Hα region was 13 000. Standard initial reduction (bias subtraction, flat-fielding and wavelength calibration) was carried out using modified *IRAF* packages (MW).

(iii) At the Crimean Astrophysical Observatory with the 2.6 m Shajn telescope, using a *SPEM* slit spectrograph mounted at the Nasmith focus. The detector was a SPEC-10 CCD camera with the 1340×100 pixels chip. Average resolution was R = 1000. The primary reduction of the spectra, including the bias subtraction and flat fielding, was performed with the *SPERED* code developed by S.I. Sergeev at the Crimean Astrophysical Observatory (TNT).

(iv) At the private station in Rouen with a 0.36 m Schmidt-Cassegrain telescope (Meade) equipped with an eShel spectrograph (Shelyak, optical ber of 50 μm) mounted at the f/d5.2 focus using a reducer. The detector was an ATIK 460EX CCD camera (pixel size of 4.54 μm, binning 2×2 mode; pixel of 9.08 μm) (FT).

(v) At the Fujii Kurosaki Observatory with a 0.4 m Schmidt-Cassegrain telescope F10 (Meade), using a FBSPEC-III spectrograph and a CCD camera ML6303E(FLI) (3072×2048 pixel) as the detector (MF).

(vi) At the Santa Maria de Montmagastrell Observatory, Tàrrega (Lleida) Spain, using a Control Remote Telescope SC16 equipped with a spectrograph B60050-VI. The detector was an ATIK 460EX CCD camera (JG).

(vii) At the Observatory de la Tourbière with a 0.4 m Ritchey-Chrétien telescope (Astrosib RC400) equipped with an eShel spectrograph (Shelyak, optical fiber of 50 μm) mounted at the f/d5.5 focus. The detector was an ATIK 460EX CCD camera (pixel size of 4.54 μm, binning 2×2 mode; pixel of 9.08 μm) (OG).

(viii) At the private stations, Manhattan (Illinois) and Grand Lake (Colorado), by a 0.25 m LX200 Schmidt-Cassegrain telescope using a Shelyak Alpy 600 spectrograph. The detector was an ATIK 314L CCD camera (KG).

(ix) At the private station Mill Ridge with a 0.31 m Cassegrain telescope equipped with a classical slit spectrograph coupled with an f/d6.6 reducer to the f/d10 focus. The spectrograph was used with a 23 μm slit (2.3 arcsec) and a 1800 l/mm grating in the first order. The detector was a QSI583 (KAF8300 chip) binned 1×2 giving 0.33 Å/pixel (R = 9000 at Hα) (T. Lester).

(x) At the Observatoire de Haute-Provence with a 0.2 m Newtonian telescope (Orion N200 f/5) equipped with a Shelyak Alpy 600 spectrograph. The detector was an ATIK 460EX CCD camera (Sony ICX694 sensor, binning 1×1) (VB).

(xi) At the private station Chelles, with a 0.35 m SCT F11 (Celestron) telescope, using the eShell cross-dispersed echelle spectrograph (Shelyak) and a CCD camera ATIK 460EX with ICX694 (Sony) sensor (T. Lemoult).

(xii) At the private station in LAquila with a 0.20 m Schmidt-Cassegrain telescope f/10, a custom built spectrograph, equipped with a 600 l/mm grism. The detector was a SBIG ST-8300M CCD camera (US).

(xiii) At the Observatory de la Couyère (CALC UAI code J23) with a 0.355 m Schmidt-Cassegrain telescope (Meade ACF 14″ f/d10) equipped with an Alpy 600 Shelyak spectrograph with 23 μm slit. The detector was an ATIK 460EX CCD camera (pixel size of 4.54 μm, binning 1×1) (JM).

(xiv) At the West Challow Observatory using a 0.28 m Schmidt-Cassegrain telescope (Celestron C11) at f/5 with a LISA spectrograph (Shelyak) and SXVR-H694 CCD camera (DB).

Our optical spectroscopy was complemented with the UV/optical and far-UV spectroscopy. The former was carried out by the Faint Object Spectrograph (*FOS*) onboard the *Hubble Space Telescope* (*HST*) during November 11, 1993 (spectra: Y1JO0305T, Y1JO0308T, Y1JO0309T, Y1JO0406T) and during December 1996 (spectra: Y3CK530AT, Y3KK040FT, Y3KK040BT, Y3KK0406T, Y3KK0408T). The latter was carried out by the *Far Ultraviolet Spectroscopic Explorer* (*FUSE*) on June 5.618, 2003 (the spectrum q1110103). We used the calibrated time-tag spectrum taken through MDRS aperture in the LiF1A (988–1082 Å) channel.

Low-resolution spectra ($R \sim 500 - 1000$, Table 2), preferentially those covering the Balmer discontinuity, were used for modelling the SED. Absolute flux calibration and correctness of the spectra were verified with the aid of the (near-)simultaneous $UBVR_CI_C$ photometry and with the reduced χ^2 quantity of the resulting model. Medium-resolution spectra ($R \sim$ 11000, Table 3) served to analyse variations in the line profiles. Absolute fluxes of the used parts of the spectrum were obtained by linear interpolation between models of the two nearest low-resolution spectra. The *HST/FOS* spectra were used for modelling the SED of the UV/optical continuum, whereas the *FUSE* spectrum was used to analyse the O VI 1032 Å line. Observations were dereddened with $E_{B-V} = 0.1$ using the extinction curve of Cardelli et al. (1989) and resulting parameters were scaled to a distance of 800 pc (see Kenyon et al. 1993, and Appendix A in detail). Finally, we determine the orbital phase of the binary according to the ephemeris of the inferior conjunction of the cool giant as (see Fekel et al. 2000),

$$JD_{\rm spec.conj.} = 2\,447\,165.3(\pm48) + 818.2(\pm1.6) \times E. \quad (1)$$

Table 1. Photometric observations of AG Peg. The full table is available in electronic form via CDS.

JD 2 4...	U	B	V	R_C	I_C	Note[1]
56997.22	9.775	9.994	8.884	–	–	PP
		.....				
57281.29	7.809	8.667	7.926	6.819	6.087	CCD
57395.21	7.769	8.713	8.000	–	–	PP

[1] A charge-coupled device (CCD) or photoelectric (PP) photometry

3. Analysis and results

3.1. Photometric evolution

Figure 1 shows the *U-LC* of AG Peg, which demonstrates that its nova-like outburst terminated around 1997, when the over-

Table 2. Log of low-resolution spectroscopic observations

Date[a] yyyy/mm/dd.ddd	JD 2 4...	Region [nm]	T_{exp} [s]	R[b]	Observatory[c]
2013/10/27.087	56592.587	363-740	4267	500	(viii)
2015/06/26.955	57200.455	370-737	1936	500	(xii)
2015/07/16.926	57220.426	330-757	40	1000	(iii)
2015/07/22.977	57226.477	330-757	40	1000	(iii)
2015/07/23.937	57227.437	330-757	20	1000	(iii)
2015/07/24.973	57228.473	330-757	60	1000	(iii)
2015/08/02.014	57236.514	378-747	917	984	(vi)
2015/08/17.983	57252.483	354-831	417	695	(x)
2015/08/19.946	57254.446	333-755	90	1000	(iii)
2015/08/20.933	57255.433	331-758	30	1000	(iii)
2015/08/21.890	57256.390	329-757	90	1000	(iii)
2015/09/04.538	57270.038	355-860	500	500	(v)
2015/09/19.846	57285.346	330-758	30	1000	(iii)
2015/09/26.950	57292.450	370-740	1322	637	(xiii)
2015/10/11.539	57307.039	355-860	500	500	(v)
2015/10/12.589	57308.089	355-860	750	500	(v)
2015/10/13.442	57308.942	355-860	600	500	(v)
2015/10/19.804	57315.304	330-757	20	1000	(iii)
2015/10/21.465	57316.965	355-860	600	500	(v)
2015/10/29.724	57325.224	330-757	30	1000	(iii)
2015/10/30.682	57326.182	330-757	90	1000	(iii)
2015/11/08.037	57334.537	373-738	265	525	(viii)
2015/11/15.453	57341.953	360-860	350	500	(v)
2015/11/23.882	57350.382	378-747	344	976	(vi)
2015/11/29.790	57356.290	378-747	282	925	(vi)
2015/12/08.453	57364.953	360-860	600	500	(v)
2015/12/24.790	57381.290	390-740	1012	821	(xiv)
2016/01/02.761	57390.261	385-753	239	772	(vi)

Notes. [(a)] Start of the observation in UT, [(b)] average resolution, [c] according to the list in Sect. 2.2.

Table 3. Log of medium resolution spectroscopic observations[a]

Date[b] yyyy/mm/dd.ddd	JD 2 4...	Region [nm]	T_{exp} [s]	Observatory[d]
2006/10/18.926	54027.426	641-692	2000	(ii)
2013/08/11.900	56516.400	427-761	1885	(xi)
2013/08/29.945	56534.445	641-688	1401	(ii)
2013/09/04.843	56540.343	641-688	301	(ii)
2013/09/04.855	56540.355	466-489	801	(ii)
2013/09/27.978	56563.478	466-489	901	(ii)
2013/10/07.004	56572.504	641-688	901	(ii)
2013/10/24.874	56590.374	466-489	601	(ii)
2013/10/26.793	56592.293	466-489	2001	(ii)
2013/12/17.716	56644.216	466-489	3601	(ii)
2015/06/27.227	57200.727	601-711	2047	(ix)
2015/07/01.011	57204.511	418-731	2747	(vii)
2015/07/09.999	57213.499	422-710	3600[c]	(i)
2015/07/17.004	57220.504	422-710	3600[c]	(i)
2015/07/29.942	57233.442	421-715	1106	(iv)
2015/08/04.971	57239.471	422-710	3600[c]	(i)
2015/08/11.006	57245.506	641-688	801[c]	(ii)
2015/08/13.896	57248.396	641-688	601	(ii)
2015/08/21.896	57256.396	421-715	1262	(iv)
2015/08/21.953	57256.453	641-688	421	(ii)
2015/08/23.002	57257.502	422-710	720	(i)
2015/08/23.983	57258.483	422-710	900	(i)
2015/08/25.039	57259.539	422-710	600	(i)
2015/08/28.927	57263.427	421-715	1798	(iv)
2015/09/06.883	57272.383	421-715	684	(iv)
2015/09/10.852	57276.352	421-715	710	(iv)
2015/09/19.875	57285.375	421-715	692	(iv)
2015/09/25.837	57291.337	421-715	445	(iv)
2015/10/01.825	57297.325	421-715	1661	(iv)
2015/10/08.849	57304.349	421-715	985	(iv)
2015/10/11.779	57307.279	421-715	888	(iv)
2015/10/12.131	57307.631	600-710	1175	(ix)
2015/10/13.777	57309.277	421-715	1197	(iv)
2015/10/20.830	57316.330	421-715	678	(iv)
2015/10/25.747	57321.247	421-715	1408	(iv)
2015/10/27.780	57323.280	422-710	1440	(i)
2015/11/01.771	57328.271	421-715	579	(iv)
2015/11/01.807	57328.307	418-731	5533	(vii)
2015/11/01.817	57328.317	641-688	2001	(ii)
2015/11/01.840	57328.340	466-489	1207	(ii)
2015/11/13.749	57340.249	421-715	1271	(iv)
2015/11/25.801	57352.301	421-715	836	(iv)
2015/12/07.805	57364.305	421-715	679	(iv)
2015/12/12.803	57369.303	421-715	1214	(iv)
2015/12/23.735	57380.235	421-715	520	(iv)
2015/12/29.761	57386.261	421-715	702	(iv)
2016/01/08.720	57396.220	422-710	1800	(i)
2016/01/13.723	57401.223	421-715	1458	(iv)

Notes. [a] Average resolution is 11000, [b] start of the observation in UT, [c] Hα saturated, [d] according to the list in Sect. 2.2.

all decline ended and the orbitally related wave-like variation reached its maximum ($\Delta U \sim 1.5$ mag), varying around 9.7 mag until June 2015. The pronounced wave like variability in the optical continuum represents a distinctive photometric feature of quiescent phases of symbiotic binaries (e.g. Hoffleit 1968; Pucinskas 1970; Meinunger 1979). This periodic variation is given by apparent changes of the nebular component of radiation as a function of the orbital phase (see Fig. 3 of Skopal 2008, and Sect. 3.2.2 below). According to the STB model, these changes can be caused by the densest parts of the ionised wind from the giant, which is partially optically thick and located in between the binary components (see Skopal 2001). During outbursts stages, the major source of the nebular radiation is represented by the ionised wind from the hot component, whose emissivity is not orbitally related, but follows the mass-loss rate (see Skopal 2006). From this point of view, the increasing amplitude of the wave-like variation along the decline of AG Peg is a result of weakening of the nebular emission from the hot star's wind, which is consistent with the observed decrease of the mass-loss rate from the hot component (Sect. 1). Transition of AG Peg to quiescent phase at some point during 1995–2000 (see Fig. 1) thus triggered the accretion process – a fundamental condition for the new energetic event.

During June of 2015, AG Peg commenced a new active phase (see Figs. 1 and 2). According to B and V CCD measurements from the AAVSO database and those collected by the VSOLJ observer Hiroyuki Maehara, the brightening started on June 5.10±3.3, 2015 (JD 2 457 177.6±3.3) at $B = 9.55 \pm 0.07$ and $V = 8.45 \pm 0.06$, and reached a maximum on June 30.0±2.0, 2015 (JD 2 457 203.5±2.0) at $B = 7.68 \pm 0.05$ and $V = 7.0 \pm 0.1$ mag. A three months gradual decline was interrupted by a weaker secondary brightening by $\Delta U \approx 1$, $\Delta B \sim 0.7$ and $\Delta V \sim 0.5$ mag on October 8.5±0.5, 2015 (JD 2 457 304.0±0.5) on the time-scale of 1 day. Then, the LCs showed a plateau phase until November 23, 2015, after which the brightness gradually decreased to values similar to those prior to the secondary eruption, at the end of the observing season of AG Peg in January 2016 (see Fig. 2). Such evolution in the multicolour LC of symbiotic binaries (brightening, timescale, and multiplicity) is classified as the Z And-type outburst.

Table 4. Parameters from model SEDs: ST, T_e (K), EM (10^{60} cm^{-3}) and a minimum of the χ^2_{red} function (see Sect. 3.2.1).

Date	ST	T_e	EM	χ^2_{red}/d.o.f.
Quiescent phase				
1993/11/13.463[a]	3.5[d]	15000	0.329	–
1996/12/12.209[b]	3.5	28000	0.188	0.630/1648
2013/10/27.087	2.6	17500	0.740	1.265/1396
Active phase				
2015/06/26.955	1.4	30000[c]	9.11	0.649/1006
2015/07/16.926	1.4	23500	5.93	1.410/1689
2015/07/22.977	2.2	22000	4.69	1.193/1618
2015/07/23.937	1.5	26500	4.72	0.739/1468
2015/07/24.973	2.3	22000	4.57	1.118/1667
2015/08/02.014	1.7	26000[c]	3.91	0.841/3720
2015/08/17.983	1.8	21000	1.89	1.183/6091
2015/08/19.946	1.8	19500	2.42	1.518/1536
2015/08/20.933	2.5	19000	2.35	1.163/1544
2015/08/21.890	2.3	19500	2.36	1.693/1590
2015/09/04.538	2.1	19500[c]	2.14	1.073/901
2015/09/19.846	2.5	20000	2.31	1.616/1685
2015/09/26.950	1.7	22000[c]	2.32	0.790/4835
2015/10/11.539	1.9	24500	5.59	0.763/1062
2015/10/12.589	2.1	26000	5.89	0.881/1019
2015/10/13.442	2.1	26000	5.97	1.000/1113
2015/10/19.804	1.6	26500	4.42	0.806/1671
2015/10/21.465	1.6	26500	6.27	1.214/1053
2015/10/29.724	1.8	23500	4.78	0.938/1672
2015/10/30.682	2.3	23000	4.56	0.930/1684
2015/11/08.037	2.3[d]	23000[c]	4.33	0.930/2142
2015/11/15.453	1.9	24000	4.06	0.804/979
2015/11/23.882	2.3[d]	23000[c]	3.90	1.449/1312
2015/11/29.790	2.3[d]	23000[c]	3.19	1.020/3716
2015/12/08.453	2.3[d]	15000	2.30	0.734/1109
2015/12/24.790	2.3[d]	23000[c]	1.82	0.755/2640
2016/01/02.761	2.3[d]	19000[c]	1.53	1.275/4322

Notes. [(a)] Hot component: $T_h \equiv 1.5 \times 10^5$ K, $R_h = 0.088\,R_\odot$, $L_h = 3560\,L_\odot$; [(b)] $T_h \equiv 1.5 \times 10^5$ K, $R_h = 0.071\,R_\odot$, $L_h = 2280\,L_\odot$. [(c)] T_e estimated using the photometric flux in U; [(d)] adopted value.

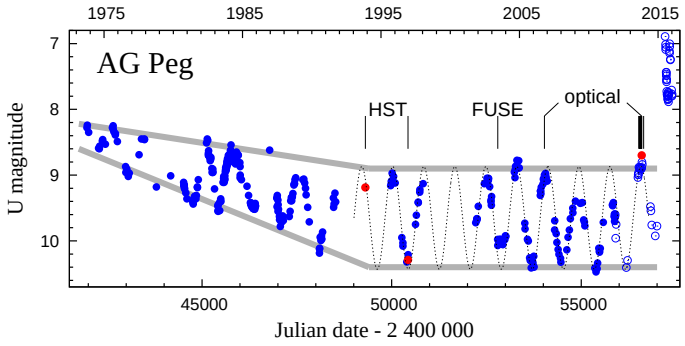

Fig. 1. The final stage of the nova-like outburst of AG Peg as demonstrated by the *U-LC* (blue dots) from 1972 to the present. Vertical lines represent timing of our spectroscopic observations during the quiescent phase. Red dots represent U magnitudes derived from model SEDs (see Sect. 3.2.2). Data are from Belyakina (1992), Mürset & Nussbaumer (1994), Hric et al. (1996), Tomov & Tomova (1998), Skopal et al. (2004), Skopal et al. (2007), Skopal et al. (2012) and this paper (⊙).

3.2. Spectroscopic evolution

In this section we determine physical parameters by modelling the continuum and analysing the line spectrum. We describe their temporal evolution along the outburst. Evolution of the main spectroscopic and physical parameters is depicted in Figs. 5 and 7. Corresponding data are included in Tables 4, 5, and 6.

3.2.1. Modelling the SED

According to properties of symbiotic stars (see Sect. 1), their observed spectrum, $F(\lambda)$, can be expressed as a superposition of its three basic components,

$$F(\lambda) = F_h(\lambda) + F_n(\lambda) + F_g(\lambda), \quad (2)$$

where $F_h(\lambda)$, $F_n(\lambda)$, and $F_g(\lambda)$ represent radiative contributions from the hot component, nebula, and giant, respectively. Because of the very high temperature of the hot component ($T_h \sim 10^5$ K, Sect. 1), we observe only its long-wavelength tail in the UV/optical range, which can be approximated by a blackbody radiation. The nebular continuum was ascribed to processes of recombination and thermal bremsstrahlung in the hydrogen plasma for Case B, because no feature of the He^+ and He^{+2} nebular continuum was recognisable in the spectrum (e.g. the 2051 Å discontinuity) and all the continua are similar in the profile (Brown & Matthews 1970). Finally, the radiation from the giant was compared with a synthetic spectrum, $\mathcal{F}_\lambda(T_{eff})$, according to models of Fluks et al. (1994). Then Eq. (2) can be expressed as (Skopal 2005b),

$$F(\lambda) = \theta_h^2 \pi B_\lambda(T_h) + k_n \varepsilon_\lambda(T_e) + \mathcal{F}_\lambda(T_{eff}), \quad (3)$$

where the angular radius of the hot component, $\theta_h = R_h/d$, is given by its effective radius, R_h (i.e. the radius of a sphere with the same luminosity) and the distance d. The factor k_n [cm^{-5}] scales the volume emission coefficient $\varepsilon_\lambda(T_e)$ [erg cm^3 s^{-1} Å^{-1}] of the nebular continuum to observations. Further, the electron temperature, T_e, and thus $\varepsilon_\lambda(T_e)$ are assumed to be constant throughout the nebula, which simplifies determination of the emission measure of the nebula to $EM = 4\pi d^2 k_n$ cm^{-3} (see Eq. (9) of Skopal 2015). Angular radius of the giant, θ_g, can be obtained from its observed bolometric flux,

$$F_g^{obs} = \int_\lambda \mathcal{F}_\lambda(T_{eff})\,d\lambda = \theta_g^2 \int_\lambda \pi B_\lambda(T_{eff})\,d\lambda = \theta_g^2 \sigma T_{eff}^4. \quad (4)$$

The variables determining the model SED are θ_h, T_h, k_n, T_e, θ_g and T_{eff}. In the SED-fitting analysis, we compared a grid of models (3) with the observed continuum, and selected the one corresponding to a minimum of the reduced χ^2 function. More details can be found in Skopal (2005b, 2015).

In modelling the UV/optical continuum from 1993 and 1996, we adopted $T_h = 150000$ K as indicated during quiescent phase (see Sect. 3.2.4). For the 1996 spectrum, we simultaneously fitted 133 continuum fluxes from 1144 to 3644 Å with 1520 flux-points from 3743 to 5635 Å. In this way we obtained parameters, θ_h, k_n, T_e and the spectral type ST (i.e. T_{eff}) of the giant according to calibration of Fluks et al. (1994). For the 1993 spectrum, we fitted only 15 continuum fluxes between 1280 and 3600 Å, because of very rich emission-line spectrum creating a bump between 2200 and 2600 Å. Here, parameters θ_h, k_n and T_e were obtained. To match also a short optical part of the spectrum ($\lambda < 4700$ Å), the synthetic spectrum from the 1996 model was

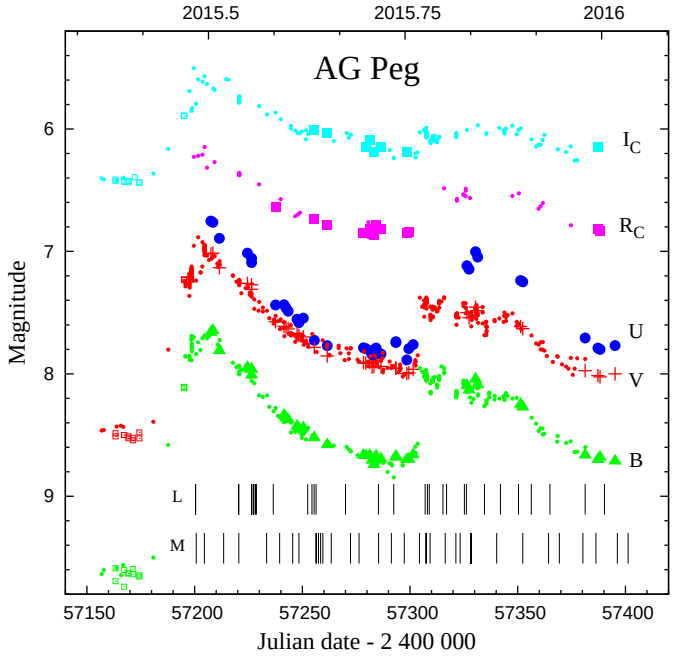

Fig. 2. U, B, V, R_C, I_C *LC*s of AG Peg during its 2015 outburst. Large symbols are our measurements (Table 1), while small ones are from the AAVSO database and those collected by the VSOLJ observer Hiroyuki Maehara (open squares prior to the brightening). Vertical bars denote the dates of our low (L) and medium (M) resolution spectra.

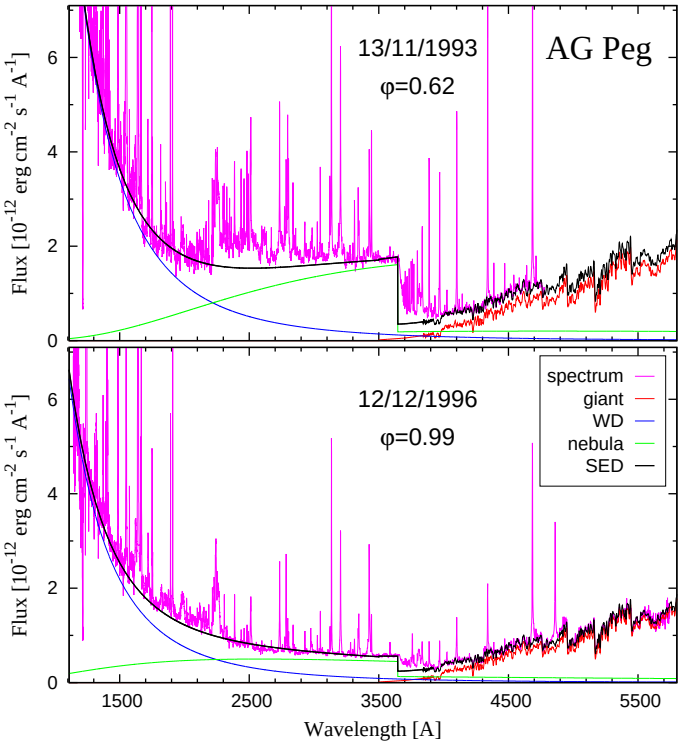

Fig. 3. UV/optical SED of AG Peg during quiescent phase from two opposite orbital phases – around the inferior and superior conjunction of the giant. This demonstrates the origin of the orbitally-related light variation in the U band shown in Fig. 1.

scaled to the observed continuum by eye. Therefore, we do not infer the value of $\chi^2_{\rm red}$ for this model SED.

To fit just the optical continuum, the method is able to disentangle contributions only from the nebula and the RG, because the WD radiation is negligibly small in the optical at the observed very high temperatures. Therefore, it was possible to determine only parameters, $k_{\rm n}$, $T_{\rm e}$, and ST. We also determined a subclass of the ST by a linear interpolation between the neighbouring best-fitting STs. Because the radiation from the giant can vary, the scaling factor of the synthetic spectra represents another parameter in the model SED.

The continuum fluxes were selected by eye. Within the optical, we distinguished the line-free regions with the aid of the synthetic spectrum of the giant. Spectral regions between the Balmer jump and ~3800 Å, from ~4720 to ~4830 Å, and from ~6860 to ~6960 Å were omitted from modelling because of blends of hydrogen emission lines, a large difference from the synthetic spectrum, and the water vapour absorptions in the Earth's atmosphere, respectively. A close comparison of the observed and synthetic spectrum revealed uncertainties of the spectral calibration to 5–10% between ~4200 and ~7100 Å, while the ends of most spectra were inclined from their model prediction up to 20% (see Fig. 4). Considering spectral ranges with a better and worse calibration, and for the sake of simplicity, we adopted uncertainties of selected continuum fluxes at all low-resolution spectra of 7%.

The resulting parameters are listed in Table 4 and examples of model SEDs are depicted in Figs. 3 and 4.

3.2.2. Emission measure

Our model SEDs revealed the presence of a strong nebular component of radiation during both the quiescent and active phase of AG Peg. It dominated the spectrum from the near-UV to around the B passband (see Figs. 3 and 4).

During quiescent phase, EM varies with the orbital phase. This is demonstrated by model SEDs of the *HST* spectra taken at the orbital phase $\varphi = 0.62$ and 0.99 (Fig. 3, Table 4). If we convert the model fluxes at the U band to the scale of the observed U magnitudes, we get an excellent agreement with the photometric U-*LC* (see the red points in Fig. 1). To get the proper quantity of the nebular contribution, we considered the emission coefficient ε_U as the weighted average of its values from both sides of the Balmer jump, $\varepsilon_U = 0.6\varepsilon_{U^-} + 0.4\varepsilon_{U^+}$ (see Cariková & Skopal 2010), multiplied by the model parameter $k_{\rm n}$ (Eq. (3)). Adding model contributions from the giant and hot component, we obtained magnitudes corresponding to the true dereddened continuum. To get the observed magnitudes, we added a correction for the emission lines, $\Delta U_l = 0.19$ mag (Skopal 2007) and the reddening of +0.48 mag in the U passband. In this way we obtained $U = 9.18$ and 10.29 for the above mentioned orbital phases. Similarly, we obtained $U \sim 8.7$ from the model SED on October 27, 2013 ($\varphi = 0.52$). This result confirms that the periodic wave-like variation in the U-*LC* of AG Peg from ~ 1997 was caused by the apparent orbital changes in the EM, similarly to variation during quiescent phases of other symbiotic stars (see Skopal 2001, and Sect. 3.1 above).

During the outburst, EM increased by a factor of ~ 10, and its quantity followed the *LC* profile (see Fig. 5). No orbitally related variation could be recognised. This implies that the large

nebular emission was produced by a different source than during quiescence. According to the ionisation structure of hot components during active phases (Cariková & Skopal 2012), and a significant broadening of the H I and He II line profiles (Fig. 6), the large *EM* was generated by the ionised wind from the hot component (Skopal 2006).

3.2.3. He II 4686 Å and Hβ lines

Basic properties of the symbiotic nebula during the outburst – the ionised wind from the hot component – can be probed by analysing recombination lines, He II 4686 Å and Hβ. The zones of their ions can be different in size, and subject to variation during the outburst. Both lines were well exposed at all our spectra. The He II λ4686 profile was more or less symmetrical, whereas the Hβ emission was attenuated by an absorption component from its blue side. Therefore, to estimate the total emission of the Hβ line, we removed the absorption component by fitting the emission core with Gaussian curves. Evolution of He II λ4686 and Hβ parameters is depicted in Fig. 5, and can be summarised as follows.

(i) During the outburst, fluxes of He II 4686 Å and Hβ lines increased by a factor of $\gtrsim 5$ with respect to values from the preceding quiescence. Their variation basically copied that in *LC*s and *EM*, but with a less steep increase during the June/July and October 2015 brightening. A significant broadening of their profiles immediately after the optical maximum is depicted in Fig. 6.

(ii) A distinctive change was observed in their broad wings. During quiescence, no broad wings in the He II 4686 Å profile were clearly seen. We measured just the core emission with HWZI$\sim 200\,\mathrm{km\,s^{-1}}$. In the Hβ profile, weak broad wings terminated at $v_\infty \approx \pm 400\,\mathrm{km\,s^{-1}}$. During the outburst, broad wings expanding to the terminal velocity $v_\infty \gtrsim 1000\,\mathrm{km\,s^{-1}}$ developed in both the lines. In the Hβ profile, v_∞ did not change significantly for the whole observing period, whereas v_∞ of He II 4686 Å was variable and, at the end of 2015, decreased to values of the quiescent phase. This suggests a variable size of the He^{+2} zone during the outburst (see Sect. 4.5 in detail).

(iii) Broadening of the whole He II 4686 Å profile (we measured its width at 0.1, 0.5 and $0.9\times I_{\max}$) was significant at/after the optical maxima. For example, the width at $0.1\times I_{\max}$ increased with a factor of ~ 3 relative to quantities of the quiescent phase. The broadening of the line correlates with the evolution in the *EM* and $\dot{M}_\mathrm{h}$ (Figs. 5 and 7), which justifies that the nebular emission was produced by the enhanced ionised wind from the WD during the outburst.

(iv) The position of the profile shifted temporarily towards negative radial velocities (RVs) with a maximum of $\sim -35\,\mathrm{km\,s^{-1}}$ just after the October brightening, and returned back to the position of its reference wavelength at the end of November 2015 (third panel from the bottom). This interesting effect is probably connected with the ionisation structure of the hot component and its evolution in the course of the outburst (see Sect. 4.8 in detail).

3.2.4. Temperature of the ionising source

Based on the fact that the presence of ions $X^{+\mathrm{i}}$ in the nebula requires the presence of photons with $h\nu > \chi_\mathrm{i}$, where χ_i is the ionisation energy necessary to ionise $X^{+(\mathrm{i}-1)}$ to $X^{+\mathrm{i}}$, Mürset & Nussbaumer (1994) found an empirical relation between the temperature of the ionising source, T_h, and the ionisation potential χ_i of the ion $X^{+\mathrm{i}}$ as

$$\frac{T_\mathrm{h}}{\chi_\mathrm{i}} = 1000\ [\mathrm{K/eV}]. \tag{5}$$

Thus the presence of an ion with the highest ionisation energy, $\chi_{\max}$, determines the lower limit of T_h. Using this approach to the spectrum of AG Peg, the presence of the O VI 1032 Å line and/or its Raman scattered counterpart at 6825 Å (see Sect. 3.2.7) requires $T_\mathrm{h} \gtrsim 114\,000$ K, because $\chi_{\max} = \chi(O^{+5}) \sim 114$ eV.

Having only optical spectra available, we can use the He II(λ4686)/Hβ flux ratio to estimate T_h. Under optically thick conditions, where the F_{4686} nebular flux growths from complete absorption of stellar photons solely by He^+ ions, $Q(4\nu_0, \infty)$, and the $F_{\mathrm{H}\beta}$ nebular flux results from complete absorption of photons between the frequency ν_0 and $4\nu_0$, $Q(\nu_0, 4\nu_0)$, a relationship for the flux ratio can be expressed as,

$$\frac{Q(4\nu_0,\infty)}{Q(\nu_0,4\nu_0)} = \frac{\alpha(\mathrm{H}\beta)}{\alpha_{4686}}\frac{\alpha_\mathrm{B}(\mathrm{He}^+)}{\alpha_\mathrm{B}(\mathrm{H}^0)}\frac{\nu_{4861}}{\nu_{4686}}\frac{F_{4686}}{F_{\mathrm{H}\beta}}, \tag{6}$$

where ν_0 is the ionising frequency of hydrogen (e.g. Gurzadyan 1997). $\alpha(\mathrm{H}\beta)$ and α_{4686} are effective recombination coefficients for the given transition, whereas $\alpha_\mathrm{B}(\mathrm{He}^+)$ and $\alpha_\mathrm{B}(\mathrm{H}^0)$ are total recombination coefficients of He^+ and H^0 for the Case B. Dominant absorption of photons by He^+ ions within the innermost He^{+2} zone is due to recombinations of He^{+2} to He^+ that produce sufficient quanta to keep the hydrogen ionised (Hummer & Seaton 1964). This procedure was first suggested by Ambartsumyan (1932) and later modified by more authors (e.g. Iijima 1981; Kaler & Jacoby 1989).

The presence of both high and low ionisation species in the spectrum of AG Peg (e.g. O VI, [Fe VII], [O III], N III, He II, H I, He I, Fe II, [O I] λ6300) suggests that its nebula is rather ionisation-bounded, that is, the stellar radiation above ν_0 (13.6 eV) is absorbed within the nebula (see Kaler & Jacoby 1989, and references therein). The right side of Eq. (6) assumes that the lines are optically thin. This, however, need not to be satisfied in the very dense symbiotic nebulae (e.g. the decrement of hydrogen Balmer lines usually departs from theoretical prediction). However, the ratio of the fluxes lowers possible deviation from the optically thin case. Applying Eq. (6) to He II(λ4686)/Hβ flux ratios in the spectrum of AG Peg (Table 6), we used recombination coefficients from Hummer & Storey (1987) for T_e = 20000 K (Table 4) and electron concentration, $n_\mathrm{e} = 10^{10}\,\mathrm{cm^{-3}}$ (see Skopal et al. 2011): $\alpha_\mathrm{B}(\mathrm{H}^0) = 1.53\times10^{-13}$, $\alpha(\mathrm{H}\beta) = 1.74\times10^{-14}$, $\alpha_\mathrm{B}(\mathrm{He}^+) = 1.02\times10^{-12}$ and $\alpha_{4686} = 1.48\times10^{-13}\,\mathrm{cm^3\,s^{-1}}$. According to possible large uncertainties of T_e and n_e, it is important to note that the ratio of α_B to α(line) depends on T_e and n_e only marginally. Equation (6) then reads as,

$$\frac{Q(4\nu_0,\infty)}{Q(\nu_0,4\nu_0)} = 0.754\times\frac{F_{4686}}{F_{\mathrm{H}\beta}}, \tag{7}$$

where the number of quanta on the left side was calculated for Planck's function. Resulting T_h runs from $\lesssim 2\times10^5$ K at the beginning of the outburst to $\sim 1.5\times10^5$ K in January 2016 (see Fig. 7 and Table 5).

During the quiescent phase, the nebula is only partly ionisation-bounded, that is, a fraction of ionising photons escapes the nebula. As the H^+ zone is always more open than the He^{+2} zone (in the sense of the STB model, see Fig. 1 of Nussbaumer & Vogel 1987), the relative fraction of the non-absorbed photons capable of ionising hydrogen will always be

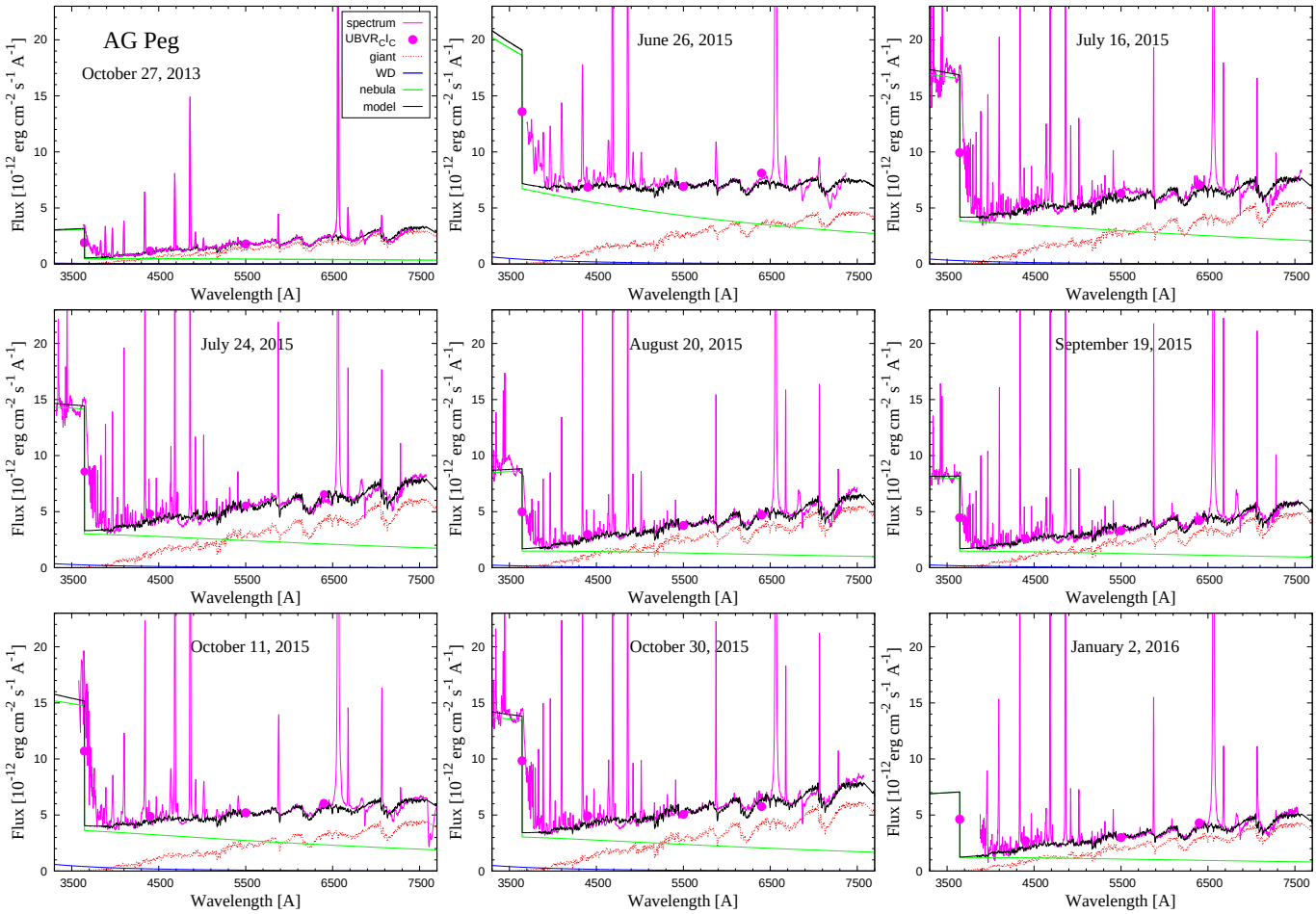

Fig. 4. Examples of our low-resolution dereddened spectra (magenta lines) and their model SEDs (black lines) at selected dates prior to and during the 2015 outburst of AG Peg. Denotation of lines is as in Fig. 3. Contribution from the WD corresponds to parameters in Table 5. It is negligibly small throughout the optical. Modelling is described in Sect. 3.2.1.

larger than that capable of ionising He^+ ions. As a result, the observed ratio $(F_{4686}/F_{H\beta})_{obs.} > F_{4686}/F_{H\beta}$ in Eq. (6). Therefore, during quiescent phases, the He II/Hβ method indicates only the upper limit of T_h. In addition, $F_{H\beta}$ and thus T_h changes with orbital phase (see Kenyon et al. 2001), because the nebula is partially optically thick (Sect. 3.1). As Eq. (6) assumes that both the lines are optically thin, maximum fluxes at $\varphi \sim 0.5$ (WD in front) correspond to the most appropriate upper limit of T_h. Our values of 156–168 kK (Table 5) that we obtained during the quiescent phase around $\varphi = 0.5$, thus represent an upper limit of T_h. Therefore, in modelling the SED during the quiescent phase (Sect. 3.2.1) we adopted a lower value of $T_h = 150000$ K.

Kaler & Jacoby (1989) used the Ambartsumyan's approach and calculated the Zanstra H I and He II temperatures. In an iteration process, forcing agreement between all temperatures, they derived the so-called 'crossover temperature', T_{cross}. For $0.08 < F_{4686}/F_{H\beta} < 1$ they determined its polynomial approximation as

$$\log(T_{cross}) = 4.905 + 1.11162\times10^{-2} I_c - 1.10692\times10^{-4} I_c^2 + 6.20572\times10^{-7} I_c^3, \quad (8)$$

where $I_c = 100\times F_{4686}/F_{H\beta}$. In this way determined values of T_h were higher than those obtained by the He II(λ4686)/Hβ method. A larger difference of 15–18% was indicated only at the beginning of the outburst (see Fig. 7).

Independently, a high T_h was suggested by Luna et al. (2015), who detected a supersoft black-body type component in the X-ray spectrum of AG Peg with kT$\sim$ 0.02 keV by the Swift satellite at the end of June 2015. However, Ramsay et al. (2016) did not mention this result, because they couldn't find strong evidence to confirm the presence of this supersoft component (Luna 2016, private communication).

3.2.5. Luminosity and radius of the ionising source

Having independently determined values of T_h and EM, we can estimate the luminosity L_h of the hot component, and thus its effective radius, R_h under the assumption that the total flux of its ionising photons, $Q(\nu_0, \infty)$, is balanced by the total rate of recombinations within the ionised volume V, that is,

$$Q(\nu_0, \infty) = \alpha_B(H^0, T_e) \int_V n_+(r) n_e(r)\, dV = \alpha_B(H^0, T_e) EM. \quad (9)$$

In this way the ionising photons are converted into the diffuse radiation, which we indicate in the spectrum as the nebular continuum and emission lines. Its amount in the continuum is given

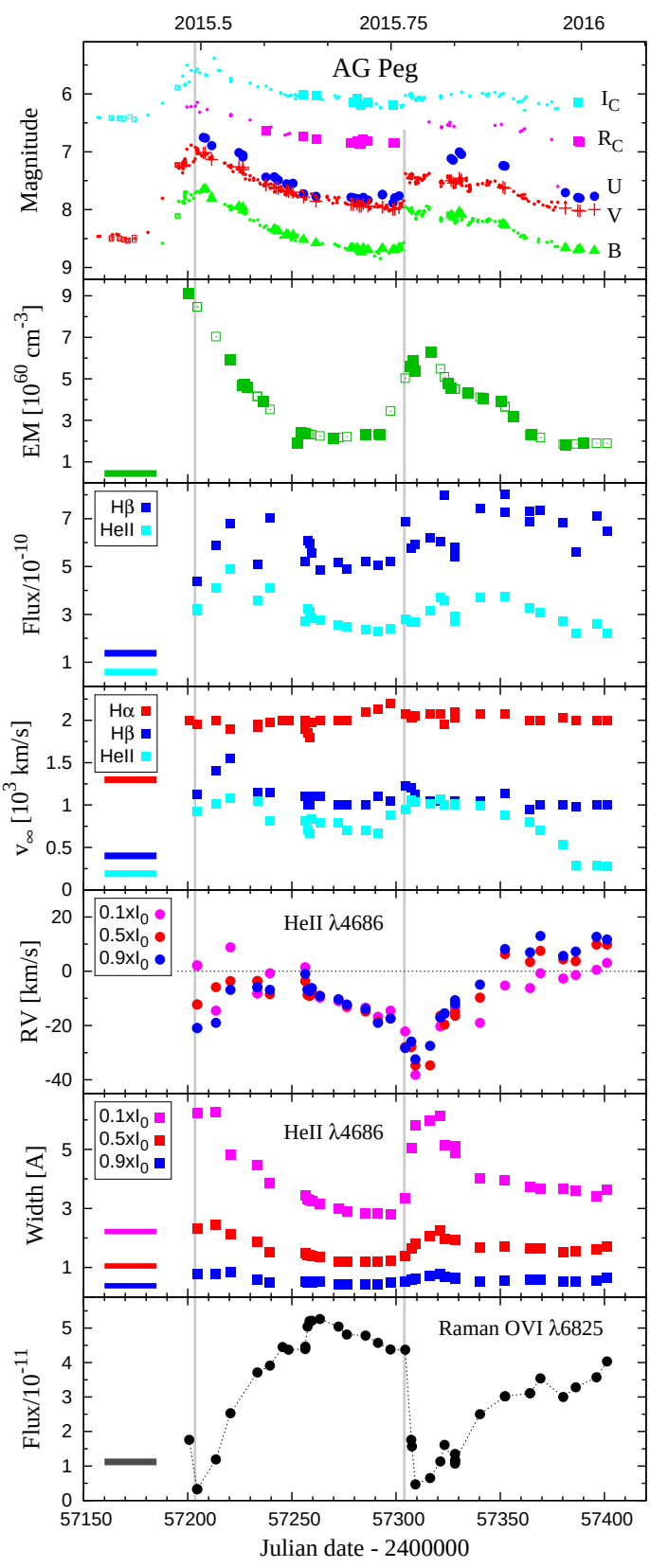

Fig. 5. Evolution of *EM* (full squares – Table 4; open squares – interpolated to dates of medium-resolution spectra) and parameters of He II λ4686, Hβ, Hα and Raman-scattered O VI λ6825 lines along the 2015 outburst of AG Peg. The horizontal belts at the bottom left corners denote the average quantity of the parameter during the preceding quiescence. Fluxes (in erg cm^{-2} s^{-1}) are listed in Table 6.

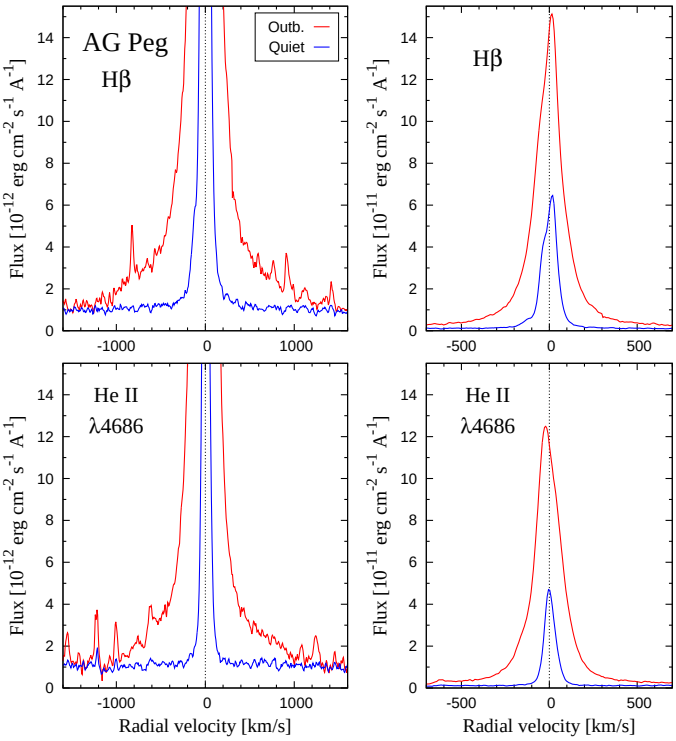

Fig. 6. Significant broadening of Hβ and He II λ4686 line profiles was observed during the outburst (red line, July 9, 2015) with respect to quiescence (blue line, October 26, 2013). Local continuum was subtracted.

by the value of *EM*, which is determined by the $F_{\rm n}(\lambda)$ component in the model SED as (see Sect. 3.2.1),

$$4\pi d^2 F_{\rm n}(\lambda) = \varepsilon_\lambda({\rm H}^0, T_{\rm e}) \int_V n_+ n_{\rm e}\, {\rm d}V = \varepsilon_\lambda({\rm H}^0, T_{\rm e}) EM. \qquad (10)$$

This includes the kinetic energy of free electrons released into the continuum via f–f and f–b transitions. Using the expression for $Q(\nu_0, \infty)$ given by Eq. (11) of Skopal (2001), the luminosity $L_{\rm h}$ of the ionising source, which generates the observed *EM*, can be expressed as

$$L_{\rm h} = \alpha_{\rm B}({\rm H}^0, T_{\rm e})\, EM \frac{\sigma T_{\rm h}^4}{f(T_{\rm h})}, \qquad (11)$$

where the function

$$f(T_{\rm h}) = \frac{\pi}{hc} \int_0^{912{\rm Å}} \lambda\, B_\lambda(T_{\rm h})\, {\rm d}\lambda \qquad (12)$$

determines the flux of ionising photons emitted by 1 cm^2 area of the hot component photosphere (cm^{-2} s^{-1}). Finally, the effective radius of the hot component, $R_{\rm h}$, is determined according to Stefan-Boltzmann law as

$$R_{\rm h} = \sqrt{\frac{L_{\rm h}}{4\pi\sigma T_{\rm h}^4}}, \qquad (13)$$

where σ is the Stefan-Boltzmann constant.

To determine $L_{\rm h}$ using $T_{\rm h}$ and *EM*, we interpolated the original values of *EM* obtained from the low-resolution spectra to dates of medium-resolution spectra (the source of $T_{\rm h}$, see Fig. 5).

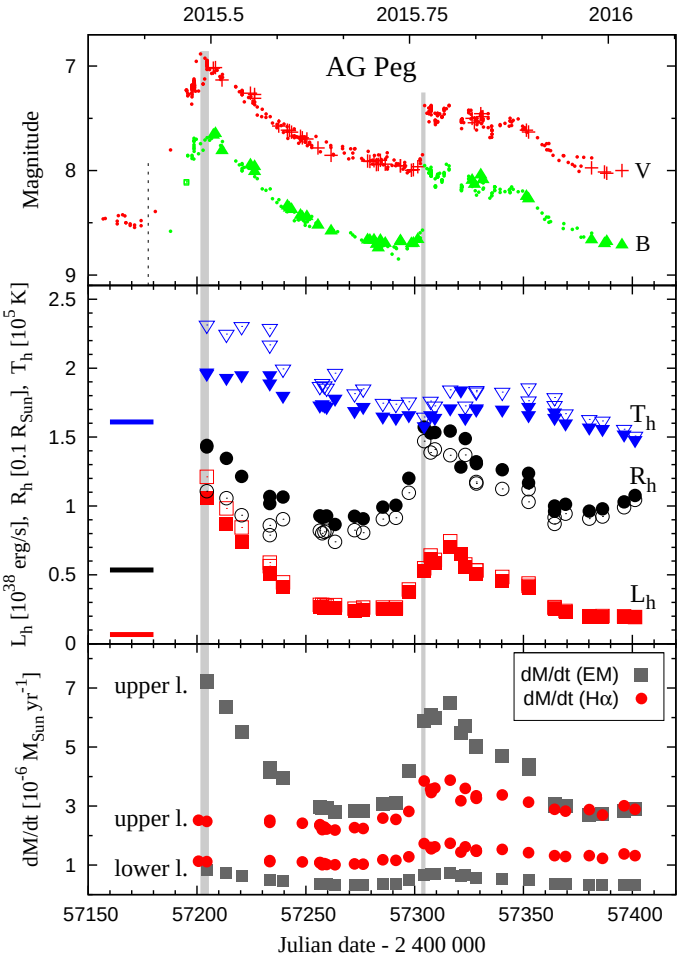

Fig. 7. Evolution of the parameters L_h, R_h, T_h (middle), and the mass-loss rate $\dot{M}_h$ from the hot component (bottom; the upper and lower limits are denoted by 'upper l.' and 'lower l.'). The dotted and grey lines mark the beginning of the explosion (June 5.10±3.3) and the maxima in the *LC* (June 30.0±2.0, Oct. 8.5±0.5). Filled and open symbols correspond to T_h from Eqs. (7) and (8). Data are listed in Table 5.

Temporal evolution of parameters T_h, R_h, and L_h along the outburst is shown in Fig. 7. Corresponding data are in Table 5.

Maximum values of all parameters correspond to the maximum of the star's brightness, because the nebular emission dominated the optical. As this component was strong and variable (Fig. 4), the evolution in the *EM* thus governed the profile of both the *LC* and other dependent parameters in the course of the outburst (see Sect. 4 in detail).

Finally, determination of the fundamental parameters, L_h, R_h and T_h (Sects. 3.2.4 and 3.2.5) was made under the assumption that the ionising source radiates as a black body. Reliability of this approach is discussed in Appendix B.

3.2.6. Mass-loss rate from the hot component

It was shown that the nebular emission during active phases of symbiotic stars is generated by the ionised stellar wind from their hot components (Skopal 2006). Hence, the significant increase of the nebular emission in the spectrum of AG Peg, in both the continuum and lines (see Figs. 5 and 6), suggests a significant increase of the mass-loss rate, $\dot{M}_h$, from its hot component in the form of ionised wind. Below we estimate $\dot{M}_h$ from the nebular continuum and the Hα emission.

We assume a spherically symmetric wind around the hot component with the beginning at the radial distance from the WD centre $r = R_0$, that becomes optically thin at $r = R_{in}$. Further, the particle velocity of the wind satisfies the β-law wind as introduced by Lamers & Cassinelli (1999),

$$v(r) = v_\infty \left(1 - \frac{bR_0}{r}\right)^\beta , \tag{14}$$

where β determines the acceleration of the wind, v_∞ is its terminal velocity, and the parameter b is given by

$$b = 1 - \left(\frac{a}{v_\infty}\right)^{1/\beta} , \tag{15}$$

where a is the initial velocity of the wind at its origin.

Mass-loss rate from the *EM*. For the ionised wind, as specified above, we can express its *EM* as (see Appendix C),

$$EM = \frac{4\pi}{(4\pi\mu m_H)^2}\left(\frac{\dot{M}_h}{v_\infty}\right)^2 \frac{1}{bR_0(1-2\beta)}\left[1 - \left(1 - \frac{bR_0}{R_{in}}\right)^{1-2\beta}\right], \tag{16}$$

where μ is the mean molecular weight and m_H is the mass of the hydrogen atom. Extension of Hα wings suggests $v_\infty \sim 2000\,\mathrm{km\,s^{-1}}$ (Fig. 5). According to a model of the broad Hα wings in the spectra of symbiotic binaries (see Skopal 2006), we adopted $\beta \sim 1.7$ and, according to Cariková & Skopal (2012), we adopted $a = 50\,\mathrm{km\,s^{-1}}$. We assume that the wind becomes optically thin in the continuum at the WD's pseudophotosphere, that is, $R_{in} = R_h$. Following the theory of the so-called optically thick wind in nova outbursts, in which the matter is accelerated deep inside the photosphere (e.g. Kato & Hachisu 1994), we can estimate the lower and the upper limit of the mass-loss rate as follows.

- If the wind begins at the WD's pseudophotosphere (= the optically thick/thin interface of the wind), that is, $R_0 = R_h$, we obtain the lower limit of $\dot{M}_h$ (see Eq. (16)). The measured values of *EM* and R_h imply $\dot{M}_h = 3.3 - 8.3 \times 10^{-7}\,M_\odot\,\mathrm{yr^{-1}}$.
- If the wind begins at the WD's surface, that is, $R_0 = R_{WD}$, Eq. (16) provides the upper limit of $\dot{M}_h$. Our measurements and $R_{WD} \equiv 0.01\,R_\odot$ correspond to $\dot{M}_h = 2.7 - 7.2 \times 10^{-6}\,M_\odot\,\mathrm{yr^{-1}}$.

In the real case, the wind probably begins somewhere between R_{WD} and R_h. For example, setting $R_0 = 0.06\,R_\odot$ results in $\dot{M}_h = 1.4 - 5.1 \times 10^{-6}\,M_\odot\,\mathrm{yr^{-1}}$. Table 5 presents the average of the upper and lower limit of $\dot{M}_h$. We note that the method is not applicable for the quiescent phase, because the corresponding *EM* represents the nebular emission from the ionised wind from the giant.

Mass-loss rate from the Hα flux. Using the same assumptions as for the continuum radiation, the measured flux in the Hα line, $F_{H\alpha}$, allows us to express its luminosity as

$$4\pi d^2 F_{H\alpha} = h\nu(H\alpha)\alpha(H\alpha, T_e) \int_{R_{in}}^{\infty} n_e(r) n_p(r)\,\mathrm{d}V, \tag{17}$$

where $\alpha(H\alpha, T_e)$ is the effective recombination coefficient for the Hα transition, and n_e and n_p is the concentration of electrons and protons in the spherical H^+ zone with the inner radius $r = R_{in}$, at which the wind becomes optically thin in the Hα line. This fundamental condition was treated by Leitherer (1988) for stellar

Table 5. Parameters of the hot component, L_h (10^{37} erg s^{-1}), R_h ($R_\odot$), T_h (10^5 K) and $\dot{M}_h$ ($10^{-6}\,M_\odot$ yr^{-1}) (see Sects. 3.2.4, 3.2.5 and 3.2.6).

Date	L_h	R_h	T_h [a)]	$\dot{M}_h$ [b)]
Quiescent phase				
2013/08/11.900	0.6±0.1	0.056±0.003	1.56±0.06	–
2013/09/04.855	0.6±0.1	0.058±0.003	1.54±0.06	–
2013/09/27.978	0.7±0.1	0.054±0.003	1.60±0.06	–
2013/10/24.874	0.7±0.1	0.053±0.003	1.62±0.06	–
2013/10/26.793	0.7±0.1	0.051±0.003	1.66±0.07	–
2013/12/17.716	0.7±0.1	0.050±0.003	1.68±0.07	–
Active phase				
2015/07/01.011	10.6±1.0	0.143±0.009	1.97±0.08	4.0
2015/07/09.999	8.7±0.8	0.135±0.008	1.93±0.08	3.5
2015/07/17.004	7.4±0.7	0.121±0.007	1.95±0.08	3.1
2015/07/29.942	5.0±0.5	0.107±0.006	1.89±0.08	2.4
2015/07/29.942	5.2±0.5	0.102±0.006	1.95±0.08	2.3
2015/08/04.971	4.1±0.4	0.106±0.006	1.80±0.07	2.2
2015/08/21.896	2.7±0.2	0.093±0.006	1.73±0.07	1.7
2015/08/23.002	2.7±0.2	0.092±0.005	1.74±0.07	1.6
2015/08/23.983	2.6±0.2	0.092±0.006	1.73±0.07	1.6
2015/08/25.039	2.6±0.2	0.093±0.006	1.72±0.07	1.6
2015/08/28.927	2.6±0.2	0.087±0.005	1.78±0.07	1.6
2015/09/06.883	2.4±0.2	0.092±0.006	1.69±0.07	1.6
2015/09/10.852	2.5±0.2	0.091±0.005	1.72±0.07	1.6
2015/09/19.875	2.5±0.2	0.099±0.006	1.65±0.07	1.7
2015/09/25.837	2.5±0.2	0.101±0.006	1.64±0.07	1.7
2015/10/01.825	3.8±0.3	0.120±0.007	1.66±0.07	2.3
2015/10/08.849	5.3±0.5	0.157±0.009	1.58±0.06	3.3
2015/10/11.779	6.1±0.6	0.153±0.009	1.66±0.07	3.4
2015/10/13.777	5.9±0.5	0.153±0.009	1.64±0.07	3.3
2015/10/20.830	7.0±0.6	0.154±0.009	1.71±0.07	3.6
2015/10/25.747	6.5±0.6	0.128±0.008	1.84±0.07	3.0
2015/10/27.780	5.5±0.5	0.149±0.009	1.64±0.07	3.2
2015/11/01.771	5.0±0.5	0.132±0.008	1.70±0.07	2.8
2015/11/01.807	5.0±0.5	0.130±0.008	1.72±0.07	2.7
2015/11/01.840	5.0±0.5	0.131±0.008	1.71±0.07	2.8
2015/11/13.749	4.6±0.4	0.126±0.008	1.70±0.07	2.6
2015/11/25.801	4.1±0.4	0.117±0.007	1.72±0.07	2.4
2015/12/07.805	2.5±0.2	0.100±0.006	1.64±0.07	1.7
2015/12/12.803	2.3±0.2	0.101±0.006	1.60±0.06	1.7
2015/12/23.735	1.9±0.2	0.096±0.006	1.57±0.06	1.5
2015/12/29.761	2.0±0.2	0.098±0.006	1.56±0.06	1.5
2016/01/08.720	2.0±0.2	0.103±0.006	1.52±0.06	1.6
2016/01/13.723	1.9±0.2	0.108±0.006	1.48±0.06	1.6

Notes. [a)] According to Eq. (7), [b)] the method is not applicable for quiescent phase.

winds of OB stars. He found that winds of O stars are optically thin from a distance $r \sim 1.5R_\star$. Also, modelling the broad Hα wings in the spectra of symbiotic stars suggested the validity of the optically thin regime from about 1.2 to 1.5 R_h (Skopal 2006). Therefore, we adopted $R_{in} = 1.5 \times R_h$.

Applying Eq. (17), with the expression for the *EM* given by Eq. (16), to our values of $F_{H\alpha}$ and R_h (Tables 5 and 6), we obtain $\dot{M}_h = 1.0 - 1.6 \times 10^{-6}\,M_\odot$ yr^{-1} for $R_0 = R_h$, and $2.2 - 3.6 \times 10^{-6}\,M_\odot$ yr^{-1} for $R_0 = 0.01\,R_\odot$. We used the volume emission coefficient $h\nu(H\alpha)\alpha(H\alpha, 20000\,K) = 1.83 \times 10^{-25}$ erg cm^{3}s^{-1}.

3.2.7. Raman-scattered O VI lines

Schmid (1989) first identified broad emission bands at 6830 Å and 7088 Å in symbiotic stars as a result of Raman-scattering of the O VI 1032 Å and 1038 Å line photons on neutral hydrogen atoms. The Raman scattered O VI features were also observed in the spectrum of AG Peg (Schmid et al. 1999, and this paper).

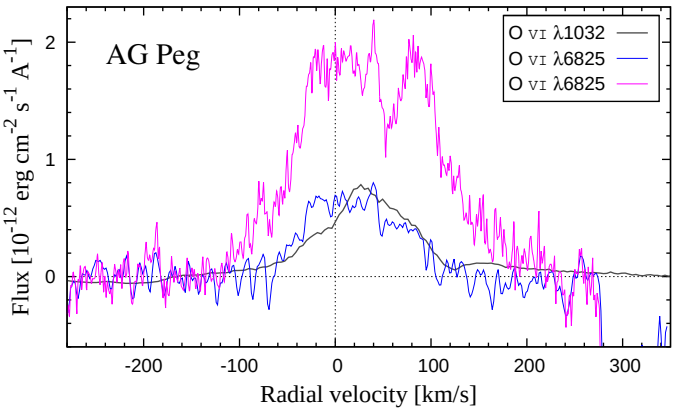

Fig. 8. Example of the Raman scattered O VI 6825 Å line during the quiescent phase (blue line; August 29.945, 2013) and the outburst (magenta line; August 28.927, 2015). Flux of the original O VI 1032 Å line (grey line; June 5.618, 2003) was scaled to that of the Raman line from quiescence. The radial velocity scale corresponds to the velocity space of the original O VI line for the systemic velocity of -16 km s^{-1} (Fekel et al. 2000) and the wavelength of the Raman transition, 6825.44 Å (Schmid 1989).

The last observation of the O VI 1032 and 1038 Å doublet was obtained with the *FUSE* satellite during quiescent phase, on June 5.618, 2003, near to the inferior conjunction of the giant ($\varphi \sim 0.9$, see Fig. 1). We estimated the observed flux of the O VI 1032 Å line to $\sim 96 \times 10^{-12}$ erg cm^{-2} s^{-1}, which corresponds to the dereddened flux of $\sim 384 \times 10^{-12}$ erg cm^{-2} s^{-1} (see Appendix B). During the quiescent phase (our spectra from 2006 and 2013), the *FWZI* of the Raman O VI 6830 Å line was 25–30 Å, and its dereddened flux of $12.5{\times}10^{-12}$ erg cm^{-2} s^{-1}. These quantities give the efficiency of the Raman scattering η ($= 6.614 \times F_{6825}/F_{1032}$) of $\sim$ 21.5%. The width of the Raman line was comparable with that measured during 1993 and 1996, whereas its dereddened flux increased by a factor of $\sim 5 - 7$ and the scattering efficiency by a factor of $\sim 3 - 5$ (see Table 7 of Schmid et al. 1999). The increase of the Raman scattering efficiency was probably caused by an enlargement of the neutral hydrogen region on the sky of the O VI zone located around the WD. This is according to the basic ionisation structure of symbiotic stars during quiescence, where the angular size of the neutral H I region, as seen from the WD, depends on the flux of ionising photons from the WD and on the flux of neutral hydrogen from the giant (STB). Since the hot component luminosity was gradually declining (see Sect. 1) and the mass-loss rate from the giant was presumably constant, the opening angle of the H I region, and thus the Raman conversion efficiency, were increasing. Also, a higher efficiency derived from the 2003 *FUSE* spectrum could be caused by measuring this spectrum at the orbital phase $\varphi \sim 0.9$, where a fraction of the original O VI photons can be attenuated by the neutral wind from the giant.

Figure 8 compares profiles of the original O VI 1032 Å line and its Raman scattered fraction. During quiescence, both profiles are nearly overlapped, except a blueward-shifted component in the Raman profile between -30 and 0 km s^{-1}. According to Schmid et al. (1999) this emission can be produced by the densest H I atoms of the giant's wind around the binary axis,

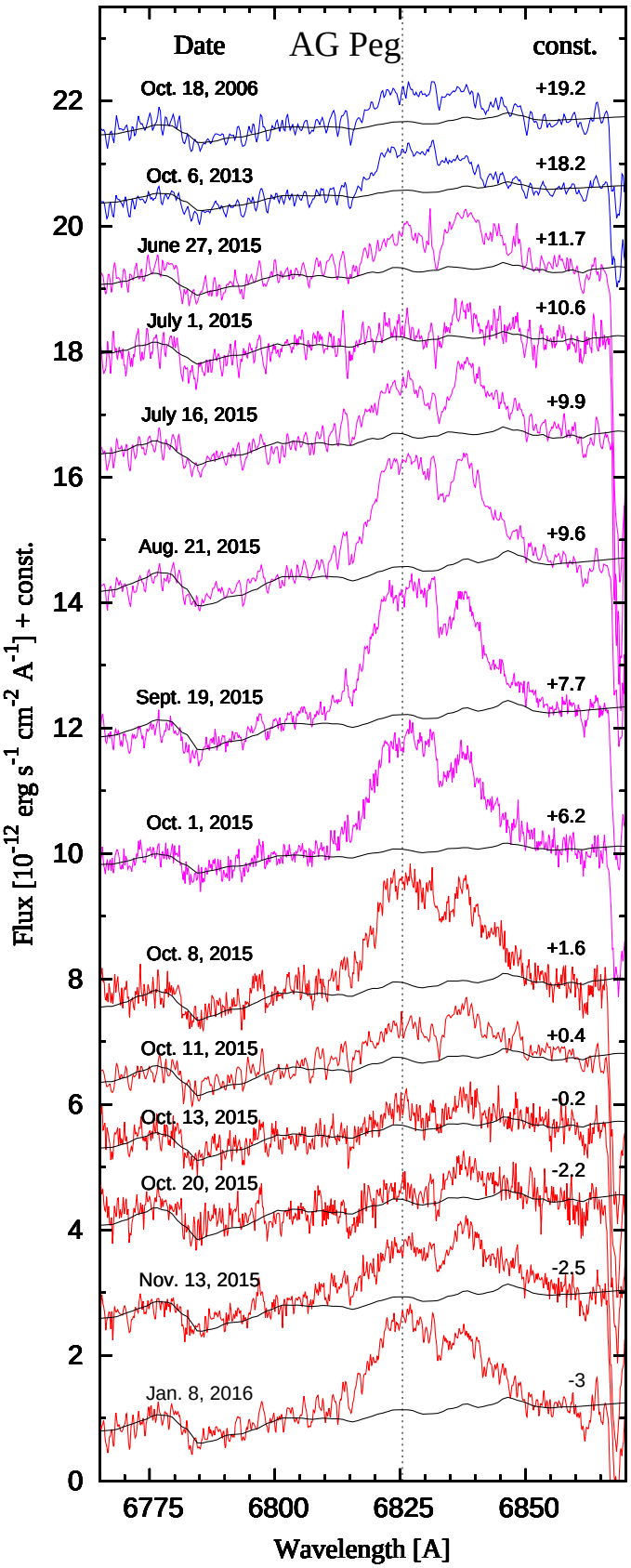

Fig. 9. Evolution of the Raman-scattered O VI 6825 Å line prior to (blue lines) and along the 2015 outburst: at/after the first maximum on June 30th (magenta lines) and the second one on October 8th (red lines). The black lines represent the continuum. Numbers on the right side mark the shift of the local continuum for a better visualisation.

that move against the O VI region. For a steep wind velocity profile of giants in symbiotic binaries, as suggested by Knill et al. (1993) and recently applied by Shagatova et al. (2016) (see their Fig. 5), the edge of this adjacent component at ~ -30 km s^{-1} can be close to the terminal velocity of the giant's wind.

During the outburst, significant variations in the Raman 6825 Å line profile were measured. Figure 5 (bottom panel) shows evolution of its fluxes, whereas Figure 9 compares its profiles along the outburst. Throughout the whole outburst, a redward-shifted component around 6838 Å developed – analogous to Z And during its 2000–2003 and 2006–2007 active phases (see Fig 4 of Skopal et al. 2006) and Fig. 5 of Skopal et al. (2009b). Except for minimum fluxes (around July 1 and October 11) the *FWZI* of the Raman line enlarged to ~ 40 Å, and its flux increased by a factor of 4–5 relative to that from the preceding quiescence. A minimum flux of the Raman line was observed just after the optical maxima (Fig. 5). Finally, a few faint absorption lines of the giant spectrum can be recognised within the Raman 6825 Å feature (e.g. at λ6807.2, λ6810.3, λ6812.5, λ6815.1, λ6824.8, λ6832.7, λ6840.0, λ6846.9 and λ6850.3). However, their influence on major features of the Raman profile is negligible.

Concerning the Raman O VI 7082 Å line, its flux was a factor of ~ 10 smaller than that of the Raman 6825 Å line during their best visibility (mid August – end of September, 2015). Also, profiles of both Raman lines were not comparable. For example, the whole blue part of the 7082 Å profile was difficult to detect (see Fig. 10). This was probably because of its weakness, and partly because the stellar spectrum is very structured around this wavelength. For example, the central part of the profile is strongly affected by an absorption at ~ 7087.5 Å. During the minimum fluxes of λ6825 Raman line, the λ7082 Raman emission was not recognisable in our spectra.

Observed variations and possible origin of the Raman 6825 Å emission during the outburst of AG Peg is discussed in Sect. 4.7.

4. Discussion

4.1. The hot component temperature

Following ionisation structure of hot components in symbiotic binaries during active phases, the high temperature of the WD's pseudophotosphere results from a low orbital inclination of AG Peg. In this case the observer can directly see the hot component in contrast to systems with high orbital inclination, when its hard radiation is blocked by the optically thick disk-like pseudophotosphere, which develops during outbursts (Skopal 2005b). Our values of 150 – 230 kK are comparable to those indicated in other symbiotic systems with the observed supersoft X-ray and far-UV fluxes generated by the WD's pseudophotosphere. For example, AG Dra (115–180 kK, Greiner et al. 1997; Skopal et al. 2009a), RR Tel (150–180 kK, González-Riestra et al. 2013), and LIN 358 (250±10 kK, Skopal 2015).

To estimate $T_{\rm h}$, Ramsay et al. (2016) used only equivalent widths of He II 4686 Å and Hβ lines, instead of their fluxes. Despite variation of the continuum level by an amplitude of ~ 1 mag in the *BV* passbands over the course of the outburst, the authors obtained values of $T_{\rm h}$ between ~1.8 and ~ 1.4×10^5 K, which are comparable with our quantities. Similar temperatures were also achieved by Tomov et al. (2016) using the same approach to their high-resolution spectra. This is the result of a

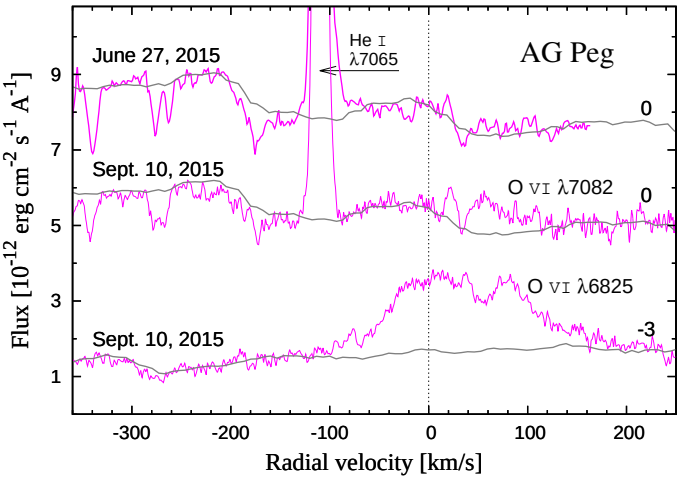

Fig. 10. Example of the Raman scattered O VI 7082 Å line around its minimum (top) and maximum flux (middle). Compared is the Raman O VI 6825 Å line (bottom). The grey line represents the continuum according to model SEDs. Radial velocity scale corresponds to the systemic velocity space of the original O VI 1031.928 or 1037.618 Å line and wavelengths of their Raman transitions at 6825.44 or 7082.40 Å.

close vicinity of both the lines in the spectrum ($\Delta\lambda \sim 175$ Å) and the method that uses their ratio.

4.2. The hot component luminosity

The high luminosity of the hot component in AG Peg of a few times 10^{37} erg s^{-1}, with a maximum of $\sim 10^{38}$ erg s^{-1}, is a natural consequence of the high value of the *EM*, measured during the 2015 outburst. For example, $EM = 5$–9×10^{60} cm^{-3} requires the rate of hydrogen-ionising photons, $Q(\nu_0,\infty) = \alpha_B(T_e) \times EM \sim 10^{48}$ s^{-1} for $\alpha_B(20000) = 1.53 \times 10^{-13}$ cm^3 s^{-1} (see Sect. 3.2.4). Such a high rate of $Q(\nu_0,\infty)$ photons requires a powerful source of radiation with L_h between 10^{37} and 10^{38} erg s^{-1}. For the WD's mass of $\sim 0.6\,M_\odot$ (Kenyon et al. 1993), the maximum luminosity of the hot component could temporarily exceed its Eddington limit.

To determine L_h during the 2015 outburst of AG Peg, Tomov et al. (2016) used, in principle, the same approach, but for emission lines. Their values of $4.5 - 6.6 \times 10^{36}$ erg s^{-1} are a factor of 19–3 below our values. This difference is caused by a larger opacity of the nebula in lines than in the continuum. For example, on July 8, 2015, their $F_{H\beta} = 36.3 \times 10^{-11}$ erg cm^{-2} s^{-1} corresponds to the emission measure

$$EM = 4\pi d^2 \frac{F_{H\beta}}{h\nu_\beta\,\alpha(H\beta)} = 3.9 \times 10^{59}\ \mathrm{cm}^{-3}, \qquad (18)$$

that is a factor of ~18 smaller than our value of $\sim 7.0\times10^{60}$ cm^{-3} determined by modelling the SED. Thus, using the line fluxes gives significantly lower values of L_h, because $L_h \propto EM$.

4.3. The hot component radius

During the outburst, the effective radius of the WD's pseudophotosphere, R_h, varied between ~ 0.09 and $\sim 0.15\,R_\odot$. On average, it was a factor of 2–3 larger than during quiescent phase. Maximum values were reached at/around maxima of the star's brightness. According to the adopted optically thick wind in nova outbursts (see Sect. 3.2.6), the optically thick/thin interface of the wind represents the WD's pseudophotosphere. As a consequence, the variations of its radius are caused by the variations in the mass-loss rate, $\dot{M}_h$. A correlation between R_h and $\dot{M}_h$ from the Hα flux (Fig. 7) supports the plausibility of the wind model.

4.4. The type of the 2015 outburst

Evolution of parameters L_h, R_h and T_h in the *H-R* diagram is depicted in Fig. 11. Optical maxima around July 1, 2015 and October 8, 2015 in the *LC* correspond to maxima in L_h and R_h. During both flares, T_h of the WD's photosphere was very high; in the first one, significantly higher than during quiescence. Throughout the whole outburst, the optical brightening was governed exclusively by the nebular component of radiation. This represents a rare case of outbursts produced by symbiotic binaries. Skopal (2005b) classified them as 2nd-type, and described them as being explained by a low orbital inclination of the binary, when the observer can directly see the hot WD (Fig. 12), and thus measures its very high T_h, L_h and *EM*. No warm pseudophotosphere in the optical was indicated by modelling the SED (Fig. 4) – the characteristic feature of the 1st-type of outbursts produced by systems with a high *i* (see Fig. 26 of Skopal 2005b).

4.5. The extension of the He^{+2} zone

From the middle of August to the end of September, and from November 25 to the end of the observing season of AG Peg (January 2016), a gradual noticeable increase of R_h was observed at a slow gradual decline of T_h (Figs. 7 and 11). The flux and the terminal velocity of the He II 4686 Å line was decreasing, whereas for the Hβ line these parameters did not change noticeably during these periods (Fig. 5). This implies a shrinking of the He^{+2} zone, because the wind was always characterised with the same v_∞, as indicated by a stable Hβ and Hα line profile, and with the same $\dot{M}_h$ (Fig. 7). During December 2015, the broad wings in the He II profile practically disappeared (Fig. 5).

Leedjärv et al. (2004) found a linear relation between equivalent widths of the He II 4686 Å and the Raman scattered O VI 6825 Å lines for measurements from quiescent phases and small brightenings. According to this result, the shrinkage of the He^{+2} zone suggests a shrinkage of the O^{+5} zone around the hot component in AG Peg during the above mentioned periods. Surprisingly, the flux of the O VI Raman line was a factor of 4.5–3.5 higher than during preceding quiescence (Fig. 5). This suggests a markedly higher Raman conversion efficiency in comparison with the quiescent phase. This is possible only if the H I scattering zone covers a larger fraction of the O^{+5} sky than in quiescence (see Sect. 4.7.3).

4.6. On the mass-loss rate

Section 3.2.6 presents a method for determining the $\dot{M}_h$ using the observed *EM* and Hα luminosity. The method assumes that the measured emission is produced by the optically thin part of the ionised wind from the hot component during the outburst. Dispersion in the $\dot{M}_h$ values obtained by the Hα method is lower than that derived from the *EM* (see Fig. 7). This is probably a result of a larger opacity of the wind in the Hα line than in the continuum. For example, at the maximum of *EM* the Hα flux was still increasing. From this point of view, the adopted value

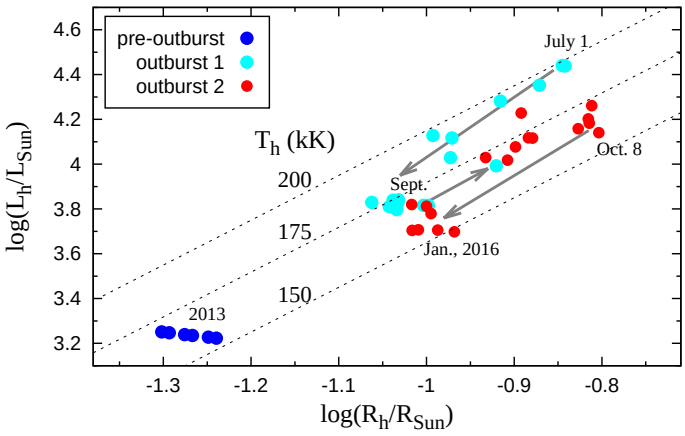

Fig. 11. Evolution of the hot component in AG Peg in the H-R diagram. Its 2015 outburst was of the 2nd-type, because of a very high temperature of the WD pseudophotosphere (see Sect. 4.4).

of the beginning of the optically thin wind in Hα, $R_{\rm in} = 1.5 \times R_{\rm h}$, is probably too rough (Sect. 3.2.6).

The upper and lower limits of the $\dot{M}_{\rm h}$ correspond to maximum uncertainty of the wind outset – at the WD's pseudophotosphere or at the WD's core surface. Their average is as high as a few $\times 10^{-6}$ $M_\odot$ yr^{-1}, which agrees with values obtained independently by fitting the broad Hα wings that develop during Z And-type outbursts of other systems (Skopal 2006)[4]. The wind is variable, because the observed nebular emission varies during the course of the outburst.

4.7. The Raman-scattered O VI *6825 Å line*

From the properties of the Raman-scattering process and its induced feature observed around 6825 Å (Figs. 8 and 9; Sect. 3.2.7) we can infer some characteristics of both the neutral H I and the ionised O VI zone during the outburst.

4.7.1. Minima of the Raman line fluxes

Fluxes of the Raman 6825 Å line, F_{6825}, are in anticorrelation with the EM and thus $\dot{M}_{\rm h}$, because $\dot{M}_{\rm h} \propto EM^{1/2}$ (Eq. (16), Figs. 5 and 7). Observing the minimum of F_{6825} fluxes at a very high temperature rejects its usual interpretation by a cooling of the ionising source. Observations suggest that the transient weakening of the O VI lines is a result of a significant increase of the $\dot{M}_{\rm h}$ (Fig. 7), which makes the O^{+5} zone optically thick, and thus more compact. For example, the optical depth of the electron-scattering layer, $\tau_{\rm e} \propto \dot{M}_{\rm h}$. Following decrease of $\dot{M}_{\rm h}$ then produces a more transparent O^{+5} zone and thus leads to an increase of both the F_{1032} and F_{6825} fluxes at similar conditions – a high $T_{\rm h}$ and the geometry of H I scatterers.

A connection between the radius of the O VI zone, $R_{\rm O\,VI}$, its $\tau_{\rm e}$, average particle density, $\bar{n}_{\rm e}$, and the EM was indicated for the symbiotic star AG Dra by Skopal et al. (2009a). Having independently determined $\tau_{\rm e}$, the authors inferred $R_{\rm O\,VI} \sim 50\,R_\odot$ ($\tau_{\rm e} = 0.061$, $\bar{n}_{\rm e} = 2.6 \times 10^{10}$ cm^{-3}, and $EM = 1.3 \times 10^{59}$ cm^{-3}) during quiescent phase, and $R_{\rm O\,VI} \sim 11\,R_\odot$ ($\tau_{\rm e} = 0.083$, $\bar{n}_{\rm e} = 1.7 \times 10^{11}$ cm^{-3}, and $EM = 2.2 \times 10^{59}$ cm^{-3}) during the transition from a burst, at high $T_{\rm h} = 1.5 - 1.6 \times 10^5$ K. However, the theoretical modelling is needed for a better understanding of the connection between $R_{\rm O\,VI}$, $\tau_{\rm e}$, $\bar{n}_{\rm e}$ and EM in the variable wind from active hot components in symbiotic binaries.

4.7.2. Broadening of the Raman line

Energy conservation of the Raman 1032 $\rightarrow$ 6825 Å conversion implies the broadening of the scattered line with a factor of $(\lambda_{\rm Ram}/\lambda_{1032})^2 \sim 44$ (Nussbaumer et al. 1989). It is given by the broadening of the original O VI line, which reflects the kinematic of emitting material in the vicinity of the hot WD, and by the relative motions between the source of the original O VI photons and the scattering H I atoms. Firstly, the observed increase of the Raman 6825 Å line width during the outburst was in part caused by a broadening of the direct O VI 1032 Å line as suggested by the broadening of He II and H I lines in the optical. Secondly, a significant change of the ionisation structure of hot components in symbiotic binaries during outbursts will produce a change in the geometry and motion of H I atoms in the binary, and thus also in the profile of the Raman-scattered lines (see below).

4.7.3. The high flux and profile of the Raman line

The significant increase of the flux, width, and development of the redward-shifted component in the profile of the Raman-scattered O VI line can be qualitatively explained by the presence of a neutral disk-like zone at the equatorial plane, which develops during active phases of symbiotic binaries around the hot WD (see Skopal 2005b; Cariková & Skopal 2012). The following points are relevant.

1. The cross-section of the λ1032 $\rightarrow$ λ6825 Raman conversion, $\sigma_{\rm Ram} \sim 5 \times 10^{-24}$ cm^2 (Lee & Lee 1997) requires the H I column density $n_{\rm H} \gtrsim 10^{23}$ cm^{-2} along the incident O VI photons to produce an observable effect (i.e. the optical depth $n_{\rm H}\sigma_{\rm Ram} \gtrsim 1$). The $n_{\rm H}$ throughout the disk-like neutral zone is of a few times $10^{22} - 10^{23}$ (see Fig 4 of Cariková & Skopal 2012), which is consistent with that needed for the O VI λ1032 Raman scattering. Thus, the O VI Raman conversion can take place mainly in the densest inner parts of the H I zone.
2. Efficiency of the Raman scattering depends on the geometry of the scattering atoms in the binary. It is proportional to the so-called covering factor $C_{\rm S} = \Delta\Omega/4\pi$, where $\Delta\Omega$ is a solid angle, under which the initial O^{+5} line photons, located mostly in the vicinity of the WD, can see the scattering region (see Lee et al. 2003). During the quiescent phase, the H I region has a cone-like shape around the giant (STB). Parameters of AG Peg suggest its opening angle of 40 – 50° (i.e. the angle between the binary axis and the asymptote to the ionisation boundary), which corresponds to $C_{\rm S} = 0.12 - 0.18$. In fact, the $C_{\rm S}$ is smaller, because the scattering region represents only part of the total H I region, which is optically thick for Raman scattering (see Sekeráš & Skopal 2015). During outbursts, location of the O^{+5} zone above/below the neutral disk suggests that the covering factor can be as high as ~ 0.5 (see Fig. 12). This makes the Raman scattering more efficient during the outburst, thus producing a strong Raman line. This interpretation is consistent with the conclusion of Sect. 4.5 that the covering factor $C_{\rm S}$ was larger than during quiescence.
3. Observations of systems with a high orbital inclination often indicate P-Cyg profiles of hydrogen Balmer lines with

[4] This method is applicable only for systems with a high orbital inclination.

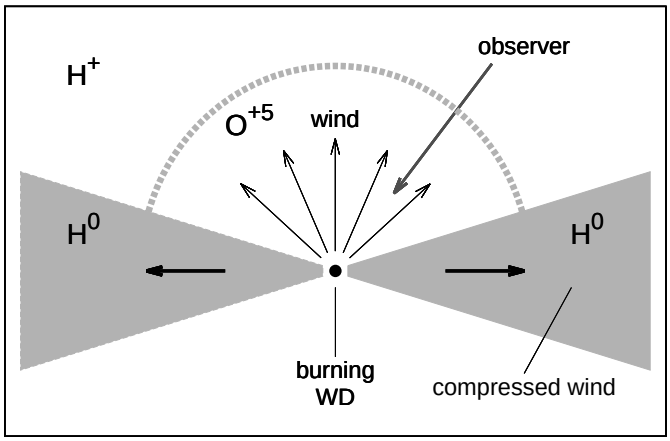

Fig. 12. Sketch of the ionisation structure of the hot component in AG Peg during its 2015 outburst (edge-on view containing the burning WD – the black circle). The enhanced wind from the WD is ionised by its radiation. Due to the rotation of the WD, the wind is compressed towards the orbital plane, where it creates a neutral H^0 zone in the form of a flared disk (see Cariková & Skopal 2012). The O^{+5} zone is bounded by the grey dashed line. Its location above/below the neutral zone significantly increases the efficiency of the Raman O VI λ1032 $\rightarrow$ λ6825 scattering process (see Sect. 4.7.3).

the absorption component at $\sim 0.1 \times v_\infty$ during outbursts. The neutral disk-like zone thus expands from the central ionising source at/around the orbital plane (see Sect. 4.1 of Skopal et al. 2006, in detail). The centrally symmetric and expanding O^{+5} wind nebular zone located above/below the neutral disk can cause a significant broadening of the Raman line during the outburst. The expanding disk-like zone of scatterers is likely to be responsible for the pronounced redward-shifted component at ~6838 Å (see Fig. 12). However, a quantitative modelling of the Raman profile during outbursts is required to approve or disapprove this theory.

The above sketched interpretation is independently supported by the presence of the Raman-scattered O VI lines in the spectrum of massive luminous B[e] star LHA 115-S 18 discovered by Torres et al. (2012). Because the B[e] supergiants may harbour dense circumstellar disks of neutral hydrogen and dust, the authors suggested that the Raman emission in the spectrum of LHA 115-S 18 could arise from such a disk illuminated by the radiation from the central hot star. Similarity of the Raman 6825 Å profile in AG Peg and in LHA 115-S 18 is striking (see Fig. 2 of Torres et al. 2012, and Fig. 9 here).

4.8. Shift and broadening of the He II emission core

During the outburst, we measured a blueward shift of the He II 4686 Å emission core with respect to its reference wavelength (Fig. 5). The effect was indicated at the beginning of the outburst, but mainly between August 23 and November 13, 2015, when the bisectors measured at 0.1, 0.5 and 0.9×$I_{\rm max}$ had similar RV (Fig. 5, third panel from the bottom). This reflected shifting of the whole line core. This effect was already indicated during outbursts of Z And (Skopal et al. 2006, 2009b), and interpreted as a result of a disk-structured hot object that blocks a fraction of the redward-shifted emission from a relatively small He^{+2} zone in the direction of the observer. As a result, the blueward shifted emission dominates the profile. The shift depends on the size of both the disk and the He^{+2} zone.

A significant shrinking of the He II zone from November 25, 2015 to January, 2016 (Sect. 4.5) with simultaneous shifting of the line core towards the reference wavelength (Fig. 5) can be interpreted as a result of a gradual dilution of the optically thick disk-like zone around the WD, signalling thus the end of the active phase.

4.9. The nature of the outburst

The high luminosity of the hot component during the quiescent phase of $\sim 2200\,L_\odot$ (Table 4) requires accretion at a rate of a few times $10^{-8}\,M_\odot\,{\rm yr}^{-1}$ to generate this luminosity by the stable hydrogen burning on the surface of a $0.6\,M_\odot$ WD (e.g. Shen & Bildsten 2007; Nomoto et al. 2007). The presence of the shell burning prior to the outburst was also suggested by Ramsay et al. (2016). However, the high accretion rate requires a high mass transfer ratio (i.e. the mass accretion rate divided by the mass-loss rate from the donor). A very efficient wind mass transfer was suggested, for example, by Mohamed & Podsiadlowski (2012), for symbiotic stars with slow and dense winds. Skopal & Cariková (2015) suggested that the high wind-mass-transfer efficiency in symbiotic stars can be caused by compression of the wind from their slowly rotating giants. Direct indication of wind focusing was found by Shagatova et al. (2016) for the symbiotic binary SY Mus.

To increase the luminosity of the burning WD by a factor of ~10, to values observed around the maximum of the 2015 outburst, a transient increase of the accretion rate to $\dot{M}_{\rm acc} \sim 3 \times 10^{-7}\,M_\odot\,{\rm yr}^{-1}$ is needed to generate the luminosity due to hydrogen burning,

$$L_{\rm nucl.} = \eta X \dot{M}_{\rm acc} \sim 8 \times 10^{37}\,{\rm erg\,s}^{-1}, \quad (19)$$

where $\eta = 6.3 \times 10^{18}\,{\rm erg\,g}^{-1}$ is the energy production of 1 gram of hydrogen due to the nuclear fusion of four protons, and $X \equiv 0.7$ is the hydrogen mass fraction in the accreted matter. The required $\dot{M}_{\rm acc}$ exceeds the stable-burning limit, which leads to blowing optically thick wind from the WD (Hachisu et al. 1996). The enhanced wind is ionised by the hot WD's pseudophotosphere, and thus converts a fraction of its stellar radiation to the nebular emission. The corresponding increase of the *EM* (Fig. 4) then causes a relevant brightening in the *LC*, which we indicate as the outburst (Fig. 2).

However, the principal question remains as to the origin of this material. Probably, the red giant is responsible for a transient increase of the mass transfer ratio, which temporarily enhances $\dot{M}_{\rm acc}$. In general, Bisikalo et al. (2006) found that variations in the velocity of the wind from the giant can cause a disruption of the accretion disk, leading to the infall of a considerable amount of matter ($\sim 10^{-7}\,M_\odot$) onto the WD surface, thus inducing the outburst. For Z And, Sokoloski et al. (2006) suggested that its 2000-02 outburst was triggered by the influx of hydrogen-rich material from a dwarf-nova-like disk instability at its start that consequently enhanced nuclear shell burning on the WD.

5. Summary

We analysed primarily high cadence optical spectroscopy and multicolour photometry obtained prior to and during the first Z And-type outburst of the symbiotic nova AG Peg that began

in June of 2015. We determined the fundamental parameters L_h, R_h and T_h of the WD's pseudophotosphere and its mass-loss rate, $\dot{M}_h$, in the course of the outburst (Fig. 7). Monitoring the evolution of the He II 4686 Å, Hβ and the Raman-scattered 6825 Å line profiles allowed us to suggest the ionisation structure of the active hot component in AG Peg (Fig. 12) and to outline the nature of its outburst. The main results of our analysis may be summarised as follows.

1. The nova-like outburst of AG Peg terminated around 1997 when a wave-like orbitally-related variation in the *LC* reached its maximum amplitude and no overall change of the star's brightness was indicated until the 2015 eruption (Fig. 1). AG Peg thus entered a quiescent phase, when the WD could start to accrete from the giant's wind (Fig. 3, Sects. 3.1 and 3.2.2).
2. Evolution of the multicolour *LC*s covering the 2015 active phase of AG Peg corresponds to the outburst of the Z And-type (Fig. 2, Sect. 3.1).
3. The brightening during the outburst was caused exclusively by the increase of the nebular component of radiation (Fig. 4, Table 4). During the outburst, the *EM* increased to a few times 10^{60} cm^{-3}, that is, by a factor of ∼10 with respect to values from the quiescent phase (Fig. 5, Sect. 3.2.2).
4. Simultaneous broadening of the line profiles and the increase of fluxes of hydrogen and He II 4686 Å lines (Figs. 5 and 6) support the idea that the nebular emission was generated by the ionised wind from the hot component.
5. During the optical maximum, T_h increased to $\sim 2 \times 10^5$ K, and then gradually decreased to $\sim 1.5 \times 10^5$ K in January 2016, being comparable with values from the preceding quiescence (Figs. 7 and 11, Sect. 3.2.4).
6. During the outburst, the luminosity L_h was as high as a few times 10^{37} erg s^{-1} with a maximum of $\sim 10^{38}$ erg s^{-1}, that is, a factor of ∼10 higher than during the preceding quiescence (Fig. 7, Sects. 3.2.5 and 4.2).
7. Assuming the so-called optically thick wind in nova outbursts, we determined $\dot{M}_h$ to be of a few $\times 10^{-6}$ $M_\odot$ yr^{-1} using our values of *EM* and Hα line fluxes (Fig. 7, Sect. 3.2.6).
8. The effective radius R_h of the WD's pseudophotosphere (= the optically thick/thin interface of the wind) increased by a factor of 2–3 with respect to values from quiescence. Maximum values of $\sim 0.15\,R_\odot$ were indicated at the optical maxima (Sects. 3.2.5 and 4.3).
9. According to model SEDs, the 2015 outburst of AG Peg belongs to the 2nd-type, because the hot component radiated at higher temperature than during quiescence (Sect. 4.4, Fig. 11) and the optical brightening was caused solely by the nebular component of radiation.
10. Significant broadening and high fluxes of the Raman-scattered O VI 6825 Å line (Figs. 5, 8 and 9, Sect. 4.7.3) and probably also the blueward shift of the He II emission core (Sect. 4.8) indicated indirectly the presence of the neutral disk-like formation encompassing the WD. This finding is consistent with the ionisation structure of hot components in symbiotic stars during active phases.

To ignite the 2015 outburst of AG Peg, a transient increase in the accretion rate to $\sim 3 \times 10^{-7}\,M_\odot$ yr^{-1} was required to generate the high luminosity ($\approx L_{\rm Edd}$ for a $0.6\,M_\odot$ WD) at the initial maximum (Sect. 4.9). Such an accretion rate exceeds a critical value for the stable hydrogen burning. Under these conditions, optically thick wind will blow from the WD. At the high temperature of the ionising source, the wind converts a fraction of the WD's photospheric radiation into a strong nebular emission that dominates the optical (Fig. 4). As a result, we observe a 2 mag brightening in the *LC*, which is classified as the Z And-type of the outburst (Sect. 4.9).

However, the above sketch of the Z And-type outburst needs to be elaborated in more detail to understand its role in the evolution of accreting WDs in symbiotic stars towards their supposed final stage of SNe Ia type. In this respect, accurate quantities of the total energy output and the mass-loss rate during both quiescent phases and outbursts are required to find if the mass of the WD can reach the Chandrasekhar limiting mass.

Acknowledgements. We thank the anonymous referee for constructive comments. Daniela Korčáková, Jan Čechura, Jakub Juryšek, Radek Kříček and Petr Zasche are thanked for their assistance in acquisition of some spectra at the Ondřejov observatory. Michaela Kraus is thanked for a discussion on the Raman lines in the spectrum of the B[e] star LHA 115-S 18. *HST* spectra presented in this paper were obtained from the Mikulski Archive for Space Telescopes (MAST). MAST is located at the Space Telescope Science Institute (STScI). STScI is operated by the Association of Universities for Research in Astronomy, Inc., under NASA contract NAS5-26555. The optical spectra presented in this paper were in part obtained within the *Astronomical Ring for Access to Spectroscopy (ARAS)*, an initiative promoting cooperation between professional and amateur astronomers in the field of spectroscopy, coordinated by Francois Teyssier. We also acknowledge the variable-star observations from the AAVSO International Database contributed by observers worldwide and used in this research. This work was supported by the Czech Science Foundation, grants P209/10/0715 and GA15-02112S, by the RFBR grant No. 15-02-06178 and NSh-9670.2016.2, by the Slovak Research and Development Agency under the contract No. APVV-15-0458, by the Slovak Academy of Sciences grant VEGA No. 2/0008/17 and by the realisation of the project ITMS No. 26220120029, based on the supporting operational Research and development program financed from the European Regional Development Fund.

References

Allen, D. A. 1980, MNRAS, 192, 521
Altamore, A., & Cassatella, A. 1997, A&A, 317, 712
Ambartsumyan, V. A. 1932, Pulkovo Obs. Circ., 4, 8
van Belle, Lane, B. F., Thomson, R. R., Boden, A. F., et al. 1999, AJ, 117, 521
Belyakina, T. S. 1992, Izv. Krym. Astrofiz. Obs., 84, 49
Bessel, M. S. 1979, PASP, 91, 589
Bisikalo, D. V., Boyarchuck, A. A., Kilpio, E. Yu., Tomov, N. A., Tomova, M. T. 2006, Astronomy Reports, 80, 722
Boffin, H. M. J., Hillen, M., Berger, J. P. et al. 2014, A&A, 564, A1
Boyarchuk, A. A. 1967, SvA, 11, 8
Brown, R. L., & Matthews, W. G. 1970, ApJ, 160, 939
Cardelli, J. A., Clayton, G. C., & Mathis, J. S. 1989, ApJ, 345, 245
Cariková, Z., & Skopal, A. 2010, NewA, 15, 637
Cariková, Z., & Skopal, A. 2012, A&A, 548, A21
Contini, M. 1997, ApJ, 483, 898
Contini, M. 2003, MNRAS, 339, 125
Dumm, T., Schmutz, W., Schild, H., & Nussbaumer, H. 1999, A&A, 349, 169
Eriksson, M., Johansson, S., & Wahlgren, G. M. 2004, A&A, 422, 987
Fekel, F. C., Joyce, R. R., Hinkle, K. H., & Skrutskie, M. F. 2000, AJ, 119, 1375
Fernández-Castro, T., Cassatella, A., Giménez, A., & Viotti, R. 1988, ApJ, 324, 1016
Fluks, M. A., Plez, B., The, P. S., de Winter, D., Westerlund, B. E., & Steenman, H. C. 1994, A&AS, 105, 311
González-Riestra, R., Selvelli, P., & Cassatella, A. 2013, A&A, 556, A85
Gregory, P. C., & Kwok, S. 1977, ApJ, 211, 429.
Greiner, J. Bickert, K., Luthardt, R., Viotti, R., Altamore, A. Gonzalez-Riestra, R., Stencel, R. E. 1997, A&A, 322, 576
Gurzadyan G. A., 1997, The Physics and Dynamics of Planetary Nebulae. Springer-Verlag, Berlin
Hachisu, I., & Kato, M. 2001, ApJ, 558, 323
Hachisu, I., Kato, M., & Nomoto, K. 1996, ApJ, 470, L97
Henden, A. A., & Kaitchuck, R. H. 1982, Astronomical Photometry, (New York: Van Nostrand Reinhold Company), 50
Henden, A. A., & Munari, U. 2006, A&A, 458, 339
Hummer, D. G., & Seaton, M. J. 1964, MNRAS, 127, 217
Hummer, D. G. & Storey, P. J. 1987, MNRAS, 224, 801
Hoffleit, D. 1968, Irish Astr. J., 8, 149
Hric, L., Skopal, A., Urban, Z., et al. 1996, CoSka, 26, 121

Iijima, T. 1981, in: Photometric and Spectroscopic Binary Systems, Proceedings of the NATO Advanced Study Institute, E. B. Carling and Z. Kopal eds. Dordrecht: D. Reidel Publishing Co., p. 517
Kaler, J. B., & Jacoby, G. H. 1989, ApJ, 345, 871
Kato, M., & Hachisu, I. 1994, ApJ, 437, 802
Kenny, H. T., Taylor, A. R., & Seaquist, E. R. 1991, ApJ, 366, 549
Kenny, H. T., & Taylor, A. R. 2007, ApJ, 662, 1231
Kenyon, S. J., & Fernández-Castro, T. 1987, AJ, 93, 938
Kenyon, S. J., Mikolajewska, J., Mikolajewski, M., Polidan, R. S., & Slovak, M. H. 1993, AJ, 106, 1573
Kenyon, S. J., Proga, D., & Keyes, Ch. D. 2001, AJ, 122, 349
Keyes, Ch. D., & Preblich, B. 2004, AJ, 128, 2981
Knill, O., Dgani, R., & Vogel, M. 1993, A&A, 274, 1002
Lamers, H. J. G. L. M., Cassinelli, J. P. 1999, Introduction to stellar winds, Cambridge University Press
Lee, H.-W., & Lee, K. W. 1997, MNRAS, 287, 211
Lee, H.-W., Sohn, Y.-J., Kang, Y. W., & Kim, H.-I. 2003, ApJ, 598, 553
Leedjärv, L., Burmeister, M., Mikołajewski, M., Puss, A., Annuk, K., Gałan, C., 2004, A&A, 415, 273
Leitherer, C. 1988, ApJ, 326, 356
Livio, M., Prialnik, D., & Regev, O. 1989, ApJ, 341, 299
Luna, G. J. M., Nunez, N. E., Sokoloski, J. L., & Montane, B. 2015, ATel. No. 7741
Lundmark, K. 1921 AN, 213,93
Meinunger, L. 1979, IBVS No. 1611
Mikolajewska, J. 2011, arXiv:1011.5657v2
Mohamed, S., & Podsiadlowski, Ph. 2012, Baltic Astronomy 21, 88
Mukai, K., Luna, G. J. M. Cusumano, G., et al. 2016, MNRAS, 461, L1
Munari, U. 1997, in Physical Processes in Symbiotic Binaries, ed. J. Mikolajewska (Warsaw: Copernicus Foundation for Polish Astronomy), 37
Mürset, U., Nussbaumer, H., Schmid, H. M., & Vogel, M. 1991, A&A, 248, 458
Mürset, U. & Nussbaumer, H. 1994, A&A, 282, 586
Mürset, U., Jordan, S., & Walder, R. 1995, A&A, 297, L87
Mürset, U., & Schmid, H. M. 1999, A&AS, 137, 473
Nomoto, K., Saio, H., Kato, M., & Hachisu, I. 2007, ApJ, 663, 1269
Nuñez, N. E., & Luna, G. J. M. 2013, ATel No. 5323
Nussbaumer, H., & Vogel, M. 1987, A&A, 182, 51
Nussbaumer, H., Schmid, H. M., Vogel, M. 1989, A&A, 211, L27
Pacźynski, B., & Żytkow, A. N. 1978, ApJ, 222, 604
Paczyński, B., & Rudak, R. 1980, A&A, 82, 349
Parimucha, Š., & Vaňko, M., 2005, CoSka, 35, 35
Pereira, C. B., & Landaberry, S. J. C. 1996, AJ, 111, 1329
Pribulla, T., Garai, Z., Hambálek, Ľ, Kollár, V., et al. 2015, AN, 336, 682
Pucinskas, A. 1970, Bull. Vilniaus Univ. Astr. Obs., 27, 24
Ramsay, G., , Luna, G. J. M., Nuñez, N. E., Sokoloski, J. L. 2015, ATel No. 7779
Ramsay, G., Sokoloski, J. L., Luna, G. J. M., Nuñez, N. E. 2016, MNRAS, 461, 3599
Rauch, T. 2003, A&A, 403, 709
Schmid, H. M. 1989, A&A, 211, L31
Schmid, H. M., Krautter, J., Appenzeller, I., et al. 1999, A&A, 348, 950
Seaquist, E. R., Taylor, A. R., & Button, S. 1984, ApJ, 284, 202 (STB)
Sekeráš, M., & Skopal, A. 2015, ApJ, 812, A162
Shagatova, N., & Skopal, A., & Cariková, Z. 2016, A&A, 588, A83
Shen, K. J., & Bildsten, L. 2007, ApJ, 660, 1444
Skopal, A. 2001, A&A, 366, 157
Skopal, A. 2005a, in: The Astrophysics of Cataclysmic Variables and Related Objects, J.-M. Hameury, & J.-P. Lasota, eds., ASP Conf. Ser. 330, San Francisco: ASP, p. 463
Skopal, A. 2005b, A&A, 440, 995
Skopal, A. 2006, A&A, 457, 1003
Skopal, A. 2007, New Astron., 12, 597
Skopal, A. 2008, JAAVSO, 36, 9
Skopal, A. 2015, New Astron., 36, 116
Skopal, A., & Shagatova, N. 2012, A&A, 547, A45
Skopal, A., Pribulla, T., Vaňko, M., et al. 2004, CoSka, 34, 45
Skopal, A., Vittone, A. A., Errico, L. et al. 2006, A&A, 453, 279
Skopal, A., Vaňko, M., Pribulla, T., et al. 2007, AN, 328, 909
Skopal, A., Sekeráš, M., González-Riestra, R., & Viotti, R. F. 2009a, A&A, 507, 1531
Skopal, A., Pribulla, T., Budaj, J., et al. 2009b, ApJ, 690, 1222
Skopal, A., Tarasova, T. N., Cariková, Z., et al. 2011, A&A, 536, A27
Skopal, A., Shugarov, S., Vaňko, M., et al. 2012, AN, 333, 242
Skopal, A., & Cariková, Z. 2015, A&A, 573, A8
Sokoloski, J. L., Kenyon, S. J., Espey, B. R., et al. 2006, ApJ, 636, 1002
Steele, I. A., Jermak, H. E., Marchant, J. M., & Bates, S. D. 2015, ATel No. 7749
Tomov, N. A. 1993, Izv. Krym. Astrofiz. Obs., 88, 22
Tomov, N. A., & Tomova, M. T. 1998, IBVS No. 4574
Tomov, N. A., & Tomova, M. T. 2001, Ap&SS, 278, 311
Tomov, T. V., Stoyanov, K. A., & Zamanov, R. K. 2016, MNRAS, 462, 4435
Torres, A. F., Kraus, M., Cidale, L. S., Barbá, R., Borges Fernandes, M., & Brandi, E. 2012, MNRAS, 427, L80
Tutukov, A. V., & Yungel'son, L. R. 1976, Astrofizika, 12, 521
Vaňko, M., Komžík, R., Kollár, V., & Sekeráš, M. 2015, CoSka, 44, 77
Vaňko, M., Komžík, R., Kollár, V., & Sekeráš, M. 2015, CoSka, 44, 91
Vogel, M. 1991, A&A, 249, 173
Yaron, O., Prialnik, D., Shara, M.M., Kovetz, A. 2005, ApJ, 623, 398
Zamanov, R., & Tomov, N. A. 1995, The Observatory, 115, 185
Zhekov, S. A., & Tomov, T. 2016, MNRAS, 461, 286

Appendix A: The distance to AG Peg

Comparing a synthetic spectrum to the *RIJKLM* flux points of the giant in AG Peg, Skopal (2005b) determined its effective temperature $T_{\rm eff} = 3600 \pm 100$ K and angular radius $\theta_{\rm g} = 2.4 \times 10^{-9} (= R_{\rm g}/d)$, which corresponds to the flux $F_{\rm g}^{\rm obs} = 5.6 \times 10^{-8}$ erg cm^{-2} s^{-1} (see Eq. (4)). Independently, Boffin et al. (2014) measured the interferometric diameter of the giant in AG Peg to 1.00 ± 0.04 mas, which yields the same $\theta_{\rm g} = 2.42 \times 10^{-9}$ and $T_{\rm eff} = 3550 \pm 120$ K for the given J and K magnitudes. Using these parameters, elements of the spectroscopic orbit and considering a radius-luminosity relation, Boffin et al. (2014) derived the parameters of the system for the orbital inclination $i = 90$, 50 and 30° (see their Table 3). For the rotational velocity of $v \sin(i) = 8.5 \pm 1.5$ km s^{-1}, mass of the WD of $0.46 \pm 0.1\, M_\odot$ and the assumption of synchronism they preferred solutions for $i = 90°$, which correspond to the distance $d = 910 - 1220$ pc.

However, $i \ll 90°$, because there is no Rayleigh scattering attenuation of the continuum around Ly-α at $\varphi \sim 0$ (see e.g. *IUE* spectra SWP03830, SWP52386 and/or the *HST* spectrum here, taken at $\varphi = 0.99$), which is always measured for eclipsing symbiotic stars during quiescent phases (see Vogel 1991; Dumm et al. 1999; Pereira & Landaberry 1996, for EG And, SY Mus, RW Hya and BF Cyg). A constraint for i can be obtained from a similarity of the ionisation structure of symbiotic stars during quiescent phases (see Fig. 11 of Kenyon et al. (1993) for AG Peg and Fig. 7 of Fernández-Castro et al. (1988) for Z And). For Z And, Skopal & Shagatova (2012) measured a weak attenuation of the far-UV continuum by Rayleigh scattering at $\varphi = 0.96$, which restricts its i to 59±3°. This suggests that i of AG Peg can be even lower than this value, because no Rayleigh attenuation is indicated. Therefore, Boffin et al. solutions for $i = 50°$ that correspond to $d = 650 - 910$ pc and $R_{\rm g} = 71.11 - 99.01\, R_\odot$ are more appropriate than those for $i = 90°$. In addition, fundamental L, R, T parameters of the giant in AG Peg satisfy statistical relations between radii, effective temperatures and spectral types for M giants better than those given by solutions for $i = 90°$ (e.g. van Belle et al. 1999). Accordingly, for the purpose of this paper, we adopted the distance to AG Peg $d = 800$ pc as originally estimated by Kenyon et al. (1993).

Appendix B: Comparison of black body and atmosphere models for the hot component

Skopal (2015) elaborated multiwavelength modelling of the global X-ray/IR SED of supersoft X-ray sources. He found that physical parameters of the overall SED do not basically depend on the model used. A black body or an atmosphere model yields a similar luminosity for given temperature (see Sect. 4.4 there).

Top panel of Fig. B.1 shows a comparison of the black body and atmosphere models for $T_{\rm eff} \equiv T_{\rm BB} = 160000$ K scaled to the far-UV fluxes of the *HST* spectrum from December 12,

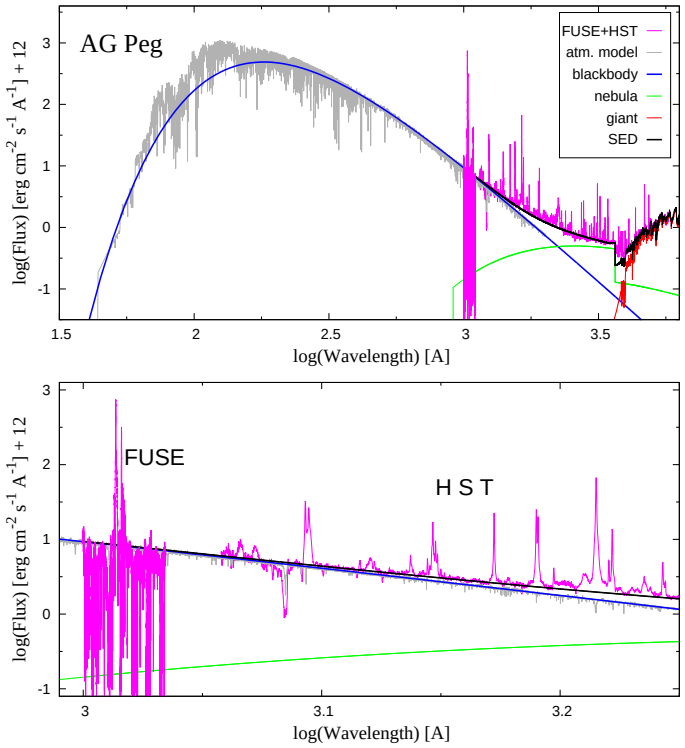

Fig. B.1. Top: Comparison of the black body and atmosphere model for 160000 K scaled to the model SED from December 12, 1996 (see Fig. 3). Bottom: A detail of the top panel between 980 and 1780 Å. Spectra were dereddened with $E_{B-V} = 0.1$ (see the text).

1996 (see Fig. 3). We used a publicly available NLTE atmosphere model described by Rauch (2003) with the H-Ni solar abundances and $\log(g) = 6$ (solid grey line). Similar profiles of the global SED for both models suggests also a similar quantity of the fluxes of ionising photons. Our illustration in Fig. B.1 corresponds to $Q(\nu_0, \infty)_{\rm atm.} = 1.57 \times 10^{47}$ and $Q(\nu_0, \infty)_{\rm BB} = 1.48 \times 10^{47}$ s^{-1}. This justifies our assumption that the hot component radiates as a black body, which we used in Sects. 3.2.4 and 3.2.5 to estimate fundamental parameters of the hot WD in AG Peg.

Bottom panel of Fig. B.1 shows the *FUSE* LiF1A channel spectrum (1000–1082 Å) from June 5, 2003, dereddened by using the far-UV extrapolation of the Cardelli et al. (1989) extinction curve. Its continuum fits well the model SED at the far-UV as given by the *HST* spectrum from December 12, 1996. We note that both spectra were obtained at similar orbital phases. This demonstrates the reliability of the extrapolation of the extinction curve to $\sim$ 1000 Å for small values of E_{B-V}. However, fluxes dereddened with $E_{B-V} = 0.3$ are a factor of 1.5–2 above the predicted model in the wavelength range of 1000–1100 Å (see Sect. 2.2. of Skopal et al. 2006, for Z And).

Appendix C: Analytical form of the *EM* for the spherically symmetric β-law wind

Emission measure of the completely ionised hydrogen in the volume V is defined as,

$$EM = \int_V n_+ n_{\rm e}\, {\rm d}V. \tag{C.1}$$

For the spherically symmetric ionised wind, whose particle density, $n(r)$, satisfies the mass continuity equation,

$$\dot{M}_{\rm h} = 4\pi\, r^2\, \mu m_{\rm H}\, n(r)\, v(r), \tag{C.2}$$

and the particle velocity, $v(r)$, obeys the β-law wind (14), the *EM* can be expressed as

$$EM = A \int_{R_{\rm in}}^{R_{\rm out}} \frac{dr}{r^2 (1 - bR_0/r)^{2\beta}}. \tag{C.3}$$

r is the radial distance from the WD centre, the stellar wind begins at $r = R_0$, $R_{\rm in}$ and $R_{\rm out}$ are the inner and outer radius of the ionized volume, respectively, and

$$A = \frac{4\pi}{(4\pi\mu m_{\rm H})^2} \left(\frac{\dot{M}_{\rm h}}{v_\infty}\right)^2. \tag{C.4}$$

Using substitutions $\sin^2(x) = bR_0/r$ and then $\cos(x) = y$, allow us to rewrite Eq. (C.3) in the analytic form,

$$EM = \frac{A}{bR_0(1-2\beta)} \left[\left(1 - \frac{bR_0}{R_{\rm out}}\right)^{1-2\beta} - \left(1 - \frac{bR_0}{R_{\rm in}}\right)^{1-2\beta} \right]. \tag{C.5}$$

For $R_{\rm out} = \infty$, Eq. (C.5) gives Eq. (16) that we used to determine $\dot{M}_{\rm h}$ from the observed *EM*. For $\beta = 0.5$,

$$EM = \frac{A}{bR_0} \left[\ln\left(1 - \frac{bR_0}{R_{\rm out}}\right) - \ln\left(1 - \frac{bR_0}{R_{\rm in}}\right) \right]. \tag{C.6}$$

Appendix D: Table of the used line fluxes

Table D.1. (= **Table 6**) Dereddened fluxes for the He II 4686 Å, Hβ, Hα and Raman scattered O VI 6825 Å lines in units of 10^{-11} erg cm^{-2} s^{-1}. $F_\lambda^{\rm obs}$ are dereddened observed fluxes, whereas $F_\lambda^{\rm tot}$ are corrected for the central absorption ($F_\lambda^{\rm tot} = F_\lambda^{\rm obs} + F_\lambda^{\rm abs}$, Sect. 3.2.3).

Date yyyy/mm/dd.ddd	Julian date JD – 2 440000	F_{4686}	$F_{\rm H\beta}^{\rm obs}$	$F_{\rm H\beta}^{\rm tot}$	$F_{\rm H\alpha}^{\rm obs}$	$F_{\rm H\alpha}^{\rm tot}$	$F_{\rm Raman}$
Quiescent phase							
2006/10/18.926	54027.426	–	–	–	47.1	52.5	1.09
2013/08/11.900	56516.400	5.24	11.9	13.5	54.4	66.4	1.21
2013/08/29.945	56534.445	-	–	–	60.8	68.6	1.34
2013/09/04.843	56540.343	-	–	–	65.8	75.1	1.33
2013/09/04.855	56540.355	5.14	11.9	13.7	–	–	–
2013/09/27.978	56563.478	5.65	11.9	13.5	–	–	–
2013/10/07.004	56572.504	-	–	–	61.1	68.8	1.27
2013/10/24.874	56590.374	6.22	12.6	14.2	–	–	–
2013/10/26.793	56592.293	6.12	11.5	13.0	–	–	–
2013/12/17.716	56644.216	7.20	12.7	14.8	–	–	–
Active phase							
2015/06/27.227	57200.727	–	–	–	140	150	1.76
2015/07/01.011	57204.511	32.2	37.1	43.9	128	152	0.33
2015/07/09.999	57213.499	40.9	51.9	58.8	sat	sat	1.19
2015/07/17.004	57220.504	48.8	58.4	68.0	sat	sat	2.53
2015/07/29.942	57233.442	35.9	45.5	50.9	195	217	3.71
2015/08/04.971	57239.471	41.1	60.0	70.5	sat	sat	3.91
2015/08/11.006	57245.506	–	–	–	sat	sat	4.45
2015/08/13.896	57248.396	–	–	–	190	216	4.37
2015/08/21.896	57256.396	27.1	43.4	52.0	192	219	4.39
2015/08/21.953	57256.453	–	–	–	201	224	4.46
2015/08/23.002	57257.502	32.3	50.2	60.7	182	197	5.04
2015/08/23.983	57258.483	31.1	48.8	59.5	189	210	5.20
2015/08/25.039	57259.539	28.6	46.1	55.5	176	197	5.21
2015/08/28.927	57263.427	27.5	39.1	48.4	186	208	5.26
2015/09/06.883	57272.383	25.5	41.1	51.7	186	207	5.04
2015/09/10.852	57276.352	25.0	37.9	48.8	173	205	4.81
2015/09/19.875	57285.375	23.8	40.2	51.9	207	249	4.78
2015/09/25.837	57291.337	23.0	41.0	50.6	204	237	4.57
2015/10/01.825	57297.325	24.2	42.9	52.2	208	239	4.38
2015/10/08.849	57304.349	28.1	54.0	68.9	290	334	4.37
2015/10/11.779	57307.279	26.9	45.2	57.6	255	295	1.76
2015/10/12.131	57307.631	–	–	–	245	283	1.57
2015/10/13.777	57309.277	26.6	46.7	59.2	255	301	0.47
2015/10/20.830	57316.330	31.4	50.8	61.8	289	346	0.65
2015/10/25.747	57321.247	37.0	52.9	60.3	246	284	1.13
2015/10/27.780	57323.280	35.8	67.0	79.8	271	309	1.61
2015/11/01.771	57328.271	29.0	48.5	57.9	260	305	1.07
2015/11/01.807	57328.307	27.2	47.6	52.9	242	295	1.35
2015/11/01.817	57328.317	–	–	–	248	294	1.16
2015/11/01.840	57328.340	27.3	47.2	54.0	–	–	1.16
2015/11/13.749	57340.249	37.2	67.6	74.4	278	325	2.50
2015/11/25.801	57352.301	37.6	69.5	72.8	274	304	3.02
2015/12/07.805	57364.305	32.9	65.3	72.9	274	308	3.11
2015/12/12.803	57369.303	30.8	62.8	73.3	260	290	3.54
2015/12/23.735	57380.235	27.3	61.1	68.5	285	317	3.00
2015/12/29.761	57386.261	22.1	50.5	56.2	245	274	3.28
2016/01/08.720	57396.220	25.8	58.7	71.0	285	323	3.57
2016/01/13.723	57401.223	21.9	54.8	64.8	254	284	4.03